

ESD ACCESSION LIST

TRI Call No. 73498
Copy No. 1 of 2 cys.

ESD RECORD COPY

RETURN TO
SCIENTIFIC & TECHNICAL INFORMATION DIVISION
(TRI), Building 1210

	1
<p style="text-align: center;">Solid State Research</p>	<p style="text-align: center;">1971</p>
<p>Prepared under Electronic Systems Division Contract F19628-70-C-0230 by</p> <p style="text-align: center;">Lincoln Laboratory</p> <p style="text-align: center;">MASSACHUSETTS INSTITUTE OF TECHNOLOGY</p> <p style="text-align: center;">Lexington, Massachusetts</p>	

AD724074

Approved for public release; distribution unlimited.

1

Solid State Research

1971

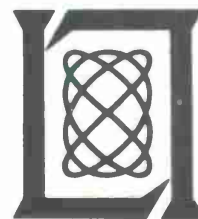
Issued 13 May 1971

Prepared under Electronic Systems Division Contract F19628-70-C-0230 by

Lincoln Laboratory

MASSACHUSETTS INSTITUTE OF TECHNOLOGY

Lexington, Massachusetts



Approved for public release; distribution unlimited.

The work reported in this document was performed at Lincoln Laboratory, a center for research operated by Massachusetts Institute of Technology, with the support of the Department of the Air Force under Contract F19628-70-C-0230.

This report may be reproduced to satisfy needs of U.S. Government agencies.

Non-Lincoln Recipients

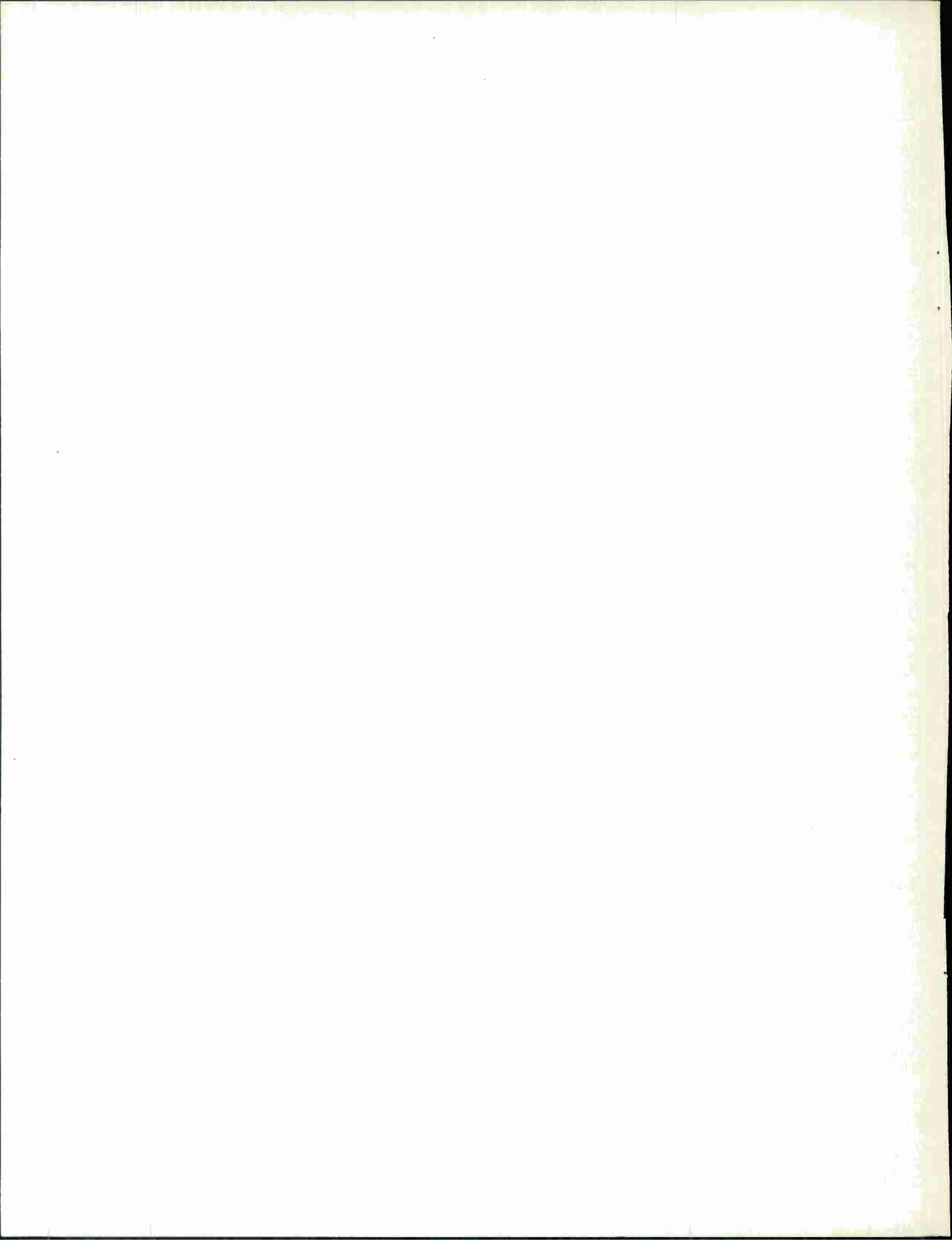
PLEASE DO NOT RETURN

Permission is given to destroy this document
when it is no longer needed.

ABSTRACT

This report covers in detail the solid state research work of the Solid State Division at Lincoln Laboratory for the period 1 November 1970 through 31 January 1971. The topics covered are Solid State Device Research, Materials Research, Physics of Solids, and Microelectronics. The Microsound work is sponsored by ABMDA and is reported under that program.

Accepted for the Air Force
Joseph R. Waterman, Lt. Col., USAF
Chief, Lincoln Laboratory Project Office



INTRODUCTION

I. SOLID STATE DEVICE RESEARCH

Proton bombardment has been used to fabricate n-p junction photovoltaic detectors from p-type PbTe and $\text{Pb}_{0.88}\text{Sn}_{0.12}\text{Te}$. Peak detectivities at $5\mu\text{m}$ as high as $3.4 \times 10^{11} \text{ cmHz}^{1/2}/\text{W}$ in reduced background have been observed in PbTe diodes at 77°K with quantum efficiencies of 36 percent. Peak detectivities of the $\text{Pb}_{0.88}\text{Sn}_{0.12}\text{Te}$ diodes at $10.2\mu\text{m}$ were as high as $1.2 \times 10^{12} \text{ cmHz}^{1/2}/\text{W}$ in reduced background at 15°K with quantum efficiencies of 37 percent.

$\text{Pb}_{0.93}\text{Sn}_{0.07}\text{Te}$ diode lasers which at 4.2°K emit continuous $8.6\text{-}\mu\text{m}$ radiation have been fabricated for high resolution spectroscopy of pollutant gases. Continuous-wave output powers up to $40\mu\text{W}$ and pulsed powers up to 10 mW have been obtained. The diodes were fabricated through an extension of the vapor growth technique used for $10.6\mu\text{m}$ $\text{Pb}_{0.88}\text{Sn}_{0.12}\text{Te}$ diode lasers by employing thallium doping.

$\text{Pb}_{1-x}\text{Sn}_x\text{Te}$ laser crystals grown by the horizontal closed-tube vapor transport process have been obtained with well-defined facets and surface areas up to 1 cm^2 . The vapor transport in this process is greatly enhanced over that of the vertical growth procedure by convection currents of the $\text{Pb}_{1-x}\text{Sn}_x\text{Te}$ vapor in the tube.

Photoluminescence studies of epitaxial GaAs in a magnetic field have shown that two acceptor levels are present in high purity material and that two free-electron neutral acceptor and two donor-acceptor pair bands are observed at low temperatures.

A simple model has been developed which demonstrates that an anomalously high apparent Hall mobility can be obtained in semiconductors containing inhomogeneities. Experimental verification of the model has been obtained by introducing high conductivity regions into epitaxial GaAs which have produced as much as a three to fivefold increase in apparent mobility. These results cast some doubt on the use of high mobility values alone as an indication of material quality unless the homogeneity can be established.

Efficient, single mode, CW, tunable spin-flip Raman laser emission has been observed in InSb, using a CO laser as a pump. External conversion efficiencies in excess of 50 percent and pump thresholds below 50 mW have been observed with the incident pump and Raman beams collinear.

II. MATERIALS RESEARCH

A method has been developed for making melting point measurements by means of thermal analysis on volatile compounds at temperatures up to about 2500°C . This method, which utilizes welded metal crucibles to contain samples, has been used to determine the melting points of EuO, EuS, EuSe, EuTe, and several other refractory compounds.

Introduction

The effect of hydrostatic pressure on the Néel temperature and ferromagnetic moment of $\text{Ca}_{1-x}\text{Sr}_x\text{MnO}_3$ has been measured for samples with $x = 0, 0.15, 0.25,$ and 0.50 . The results indicate that orthorhombic distortion decreases with pressure as well as with x and that variation of the Mn-O-Mn angle influences T_N less than variation in chemistry.

Two distinguishable mechanisms have been identified in the monoclinic-to-tetragonal transition in VO_2 : an antiferroelectric-to-paraelectric transition at a temperature T_t and a change from homopolar to metallic V-V bonding at a temperature T'_t . In pure VO_2 at atmospheric pressure, the two transitions occur at the same temperature (340°K), but a $T'_t < T_t$ may be induced by hydrostatic pressure or atomic substitutions. In the intermediate temperature range the structure is orthorhombic.

The optical absorption of n-type PbTe with carrier concentrations between 9×10^{16} and $5 \times 10^{18} \text{ cm}^{-3}$ has been measured at room temperature between 6 and $15 \mu\text{m}$. For most of the samples, the dependence of the absorption coefficient on wavelength and carrier concentration indicates that at room temperature free-carrier absorption is the dominant absorption mechanism in this wavelength range.

III. PHYSICS OF SOLIDS

The magnetic field dependence of the Hall coefficient and resistivity has been measured for p-type samples of $\text{Hg}_{1-x}\text{Cd}_x\text{Te}$, in which the energy gap was opened up from negative and very small positive values to approximately 0.06 eV by the application of hydrostatic pressure. The concentrations of electrons, heavy holes and light holes, as a function of pressure, are obtained; comparison with band model calculations yields a number of parameters including the pressure coefficient of the energy gap.

Study of the ultrasonic attenuation for bismuth in a magnetic field has been continued. Giant quantum oscillations associated with nonextremal orbits of the electrons have been unambiguously observed for the first time.

A many-body formulation of the field emission problem has been obtained, which can account for the high energy tail observed in the emission current of some materials. On the other hand, anomalies appear in the spectrum of tungsten, which seem to be due to the transient hole potential introduced when an electron tunnels out of the metal. This requires some additional modification of the theory.

A one-band model has been constructed to describe nonmetallic behavior in several limits. The limiting cases are insulating behavior due to strong correlations, band splitting accompanied by lattice distortion, and localization of small polarons at high temperatures.

Work has been initiated on an evaluation of broadband pyromagnetic detectors of the type reported by Caruthers and Walser. Simply by carefully designing the magnetic circuit and including leakage flux, we have obtained greater than an order of magnitude increase in responsivity over previous results.

Paramagnetic resonance of ferrous fluosilicate has been extended to the submillimeter region by means of HCN and DCN lasers. The new results explain the apparent discrepancy between microwave EPR and other magnetic measurements.

Our recent studies have shown that the first few terms in the high-temperature expansion for the magnetic susceptibility provide the most reliable tool for analyzing experimental susceptibility data in terms of exchange interactions. The expressions for the first five terms, previously given for a single interaction, have now been generalized to an arbitrary number of Heisenberg exchange interactions.

A qualitative explanation has been obtained for the transverse to longitudinal spin-flip transition at $T = 122^\circ\text{K}$, and the first-order nature of the antiferromagnetic transition at 312°K observed in chromium metal. These transitions occur in an extension of the Fedders-Martin model of itinerant spin density wave antiferromagnetism when the contribution of the magnetic induction to the free energy is included in the theory.

A spin wave diagrammatic approach has been developed for the temperature dependence of the line shape for two magnon Raman scattering in a simple antiferromagnet. A good description of the temperature dependence of the peak position is obtained, but in order to explain the line width, a large damping, much larger than a crude estimate yields, must be assumed for zone boundary magnons.

Study of the optical Raman scattering in FeF_2 has continued with emphasis on identifying the previously reported intense line at 1090 cm^{-1} which seemed to be related to magnetic ordering. No obvious magnetic field effects for the configuration $\text{H} \parallel \text{c}$ were observed for fields up to 88 kG; further studies will be attempted with a larger bore magnet which will permit examination with a 90° scattering geometry. Similar results were found for another sample obtained from a different source, indicating that impurity effects are probably not an important factor in the observed scattering.

A weak resonant enhancement of the Brillouin scattering cross section, less than one would predict on the basis of a theory by Loudon but greater than that expected from a simple dielectric constant approximation, is observed as the fundamental absorption edge of CdS is thermally tuned through the incident radiation at 5145 \AA . For the first time the spectral resolution is sufficient to observe an absorption-induced spread in optical wavevector resulting in line broadening. The absorption calculated from these observations is in satisfactory agreement with published transmission measurements on thin platelets.

IV. MICROELECTRONICS

The service-oriented programs have progressed rather well during this period and notable progress has been made in several major programs.

The program to explore the relationship of material properties to performance characteristics of the gallium arsenide millimeter wave diodes has provided considerable data and a number of high performance diodes.

Introduction

Large numbers of silicon wafers are being processed for oxidations and diffusions in support of the LSI program.

Several other programs involving semiconductor processing such as surface wave amplifiers, photodiode arrays, read-only memory structures, a particle detector array and TRAPATT microwave diodes have either advanced to the prototype stage or are at the point where final devices or components are being delivered.

The air-gap crossover techniques and related beam lead substrate methods are currently being applied to several service programs with excellent results.

The second generation laser scanner for integrated circuit testing is nearly complete and preliminary tests indicate greater system sensitivity has been achieved with a greater over-all reliability. New integrated circuit structures such as silicon on sapphire have been tested and evaluated with the new laser system, and further tests are under way to explore the effects of a higher power laser.

CONTENTS

Abstract	iii
Introduction	v
Reports by Authors Engaged in Solid State Research Organization	xi xviii
I. SOLID STATE DEVICE RESEARCH	1
A. N-P Junction Photovoltaic Diodes in PbTe and $\text{Pb}_{1-x}\text{Sn}_x\text{Te}$ Produced by Proton Bombardment	1
1. PbTe	1
2. $\text{Pb}_{1-x}\text{Sn}_x\text{Te}$	2
B. Continuous-Wave $\text{Pb}_{0.93}\text{Sn}_{0.07}\text{Te}$ Diode Lasers at 8.6 μm	4
C. Closed-Tube Horizontal Vapor Growth of $\text{Pb}_{1-x}\text{Sn}_x\text{Te}$ Crystals	5
D. Acceptor Luminescence in High Purity n-Type GaAs	7
E. Anomalously High "Mobility" in Semiconductors	10
F. Efficient, Single Mode, CW, Tunable Spin-Flip Raman Laser	12
II. MATERIALS RESEARCH	17
A. Sealed Crucible Technique for Thermal Analysis of Volatile Compounds up to 2500°C	17
B. Effect of Pressure on Magnetic Properties of $\text{Ca}_{1-x}\text{Sr}_x\text{MnO}_3$	21
C. Two Distinguishable Mechanisms in Semiconductor-To-Metal Transition in VO_2	23
D. Free-Carrier Absorption in n-Type PbTe	25
III. PHYSICS OF SOLIDS	29
A. Electronic Band Structure	29
1. Galvanomagnetic Measurements at Hydrostatic Pressure on $\text{Hg}_{1-x}\text{Cd}_x\text{Te}$ Alloys, near Semimetal-Semiconductor Transition	29
2. Observation of Nonextremal Fermi Surface Orbits in Bismuth	31
3. Multi-electron Field Emission	33
4. Lattice and Correlation Effects on Narrow-Band Electrons	34
B. Magnetism	34
1. Pyromagnetic Sensors	34
2. Paramagnetic Resonance in Ferrous Fluosilicate at Submillimeter Wavelengths	37
3. High-Temperature Expansion for Magnetic Susceptibility	38
4. Magnetic Phase Transition and Self-Consistent Magnetic Induction in Itinerant Antiferromagnetism	38
5. Spin Wave Approach to Two-Magnon Raman Scattering in Simple Antiferromagnet	41

C. Laser Scattering	41
1. Raman Scattering in FeF_2	41
2. Resonant Brillouin Scattering in Cadmium Sulfide	43
IV. MICROELECTRONICS	45
A. Air-Gap (Beam-Leaded) Crossovers	45
B. Silicon Nitride Deposition for SIMTOP by Reactive RF Sputtering	45
C. Metal-Based, Beam-Leaded Substrates	45
D. Semiconductor Program	46
E. Mask Facility	47
F. Programming	47
G. Bonding, Packaging and Environmental Testing	47

REPORTS BY AUTHORS ENGAGED IN SOLID STATE RESEARCH

15 November 1970 through 15 February 1971

PUBLISHED REPORTS

<u>JA No.</u>		<u>Journal Articles</u> *	
3611	Magnetic Susceptibility of Europium Trifluoride	S. Kern† P. M. Raccach A. Tveten†	J. Phys. Chem. Solids <u>31</u> , 2639 (1970)
3631	Electrical Conductivity in Narrow Energy Bands	R. A. Bari D. Adler† R. V. Lange†	Phys. Rev. B <u>2</u> , 2898 (1970)
3659A	Direct Observation of Acoustical Activity in α Quartz	A. S. Pine	Phys. Rev. B <u>2</u> , 2049 (1970)
3661	Collective Oscillations in a Simple Metal. I. Spin Waves	A. R. Wilson D. R. Fredkin†	Phys. Rev. B <u>2</u> , 4656 (1970)
3664	Magnetoreflexion Studies in Bismuth	M. Maltz† M. S. Dresselhaus	Phys. Rev. B <u>2</u> , 2877 (1970)
3682	Narrow-Band Expansions in the Hubbard Model: A Comment	R. A. Bari	Phys. Rev. B <u>2</u> , 2260 (1970)
3725	Harmonic Generation in Cold Nonuniform Plasma in a Magnetic Field	F. A. Blum	Phys. Fluids <u>14</u> , 196 (1971)
3727	Linewidths of a Gaussian Broadband Signal in a Saturated Two-Level System	M. M. Litvak	Phys. Rev. A <u>2</u> , 2107 (1970)
3730	Si_3N_4 -Masked Thermally Oxidized Post-Diffused Mesa Process (SIMTOP)	R. A. Cohen R. W. Mountain	IEEE Trans. Electron Devices <u>ED-18</u> , 54 (1971)
3737	Study of the Spin-Reordering Transition in Cr_5S_6	K. Dwight N. Menyuk J. A. Kafalas	Phys. Rev. B <u>2</u> , 3630 (1970)

* Reprints available.

† Author not at Lincoln Laboratory.

Reports

JA No.

- | | | | |
|------|---|---|--|
| 3738 | Effects of Hydrostatic Pressure and of Jahn-Teller Distortions on the Magnetic Properties of RbFeF_3 | J. B. Goodenough
N. Menyuk
K. Dwight
J. A. Kafalas | Phys. Rev. B <u>2</u> , 4640 (1970) |
| 3765 | Raman Scattering in CsMnF_3 | S. R. Chinn | Phys. Rev. B <u>3</u> , 121 (1971) |
| 3772 | Polaron Zeeman Effect of Shallow Donors in CdTe | D. R. Cohn*
D. M. Larsen
B. Lax* | Solid State Commun. <u>8</u> , 1707 (1970) |
| 3773 | Even-Parity Levels of Donors in Si | W. H. Kleiner
W. E. Krag | Phys. Rev. Letters <u>25</u> , 1490 (1970) |
| 3777 | Perturbation Theory for the Bound Polaron | D. M. Larsen | J. Phys. C <u>3</u> , L185 (1970) |
| 3787 | Polarization Modulated Magneto-reflectance in EuSe and EuTe | C. R. Pidgeon*
J. Feinleib*
T. B. Reed | Solid State Commun. <u>8</u> , 1711 (1970) |
| 3789 | Identification of Exciton-Neutral Donor Complexes in the Photoluminescence of High Purity GaAs | J. A. Rossi
C. M. Wolfe
G. E. Stillman
J. O. Dimmock | Solid State Commun. <u>8</u> , 2021 (1970) |
| 3796 | Acceptor Luminescence in High-Purity n-Type GaAs | J. A. Rossi
C. M. Wolfe
J. O. Dimmock | Phys. Rev. Letters <u>25</u> , 1614 (1970) |
| 3799 | Continuous Stimulated Spin-Flip Raman Scattering in InSb | A. Mooradian
S. R. J. Brueck
F. A. Blum | Appl. Phys. Letters <u>17</u> , 481 (1970) |
| 3814 | Absence of Hartree-Fock Behavior in Hubbard's Simple Decoupling Solution of Correlated Narrow-Energy-Band-Model | R. A. Bari
T. A. Kaplan | Phys. Letters A <u>33A</u> , 400 (1970) |

MS No.

- | | | | |
|------|--|--------------|--|
| 2847 | Magnetism | N. Menyuk | <u>Modern Aspects of Solid State Chemistry</u> , C. N. R. Rao, Ed. (Plenum Publishing Corporation New York, New York, 1970), pp. 159-217 |
| 2877 | Magneto-Optics of Polarons in Semiconductors | D. M. Larsen | Proceedings Tenth International Conference on the Physics of Semiconductors, USAEC CONF-700801 (1970), p. 145 |

* Author not at Lincoln Laboratory.

<u>MS No.</u>			
2882	Electron and Phonon Dispersion Relations in Tellurium	G. Dresselhaus M.S. Dresselhaus	<u>ibid.</u> , p. 338
2886	Interaction of Bound Electrons with Local and Resonant Modes in Semiconductors	R. W. Davies H. J. Zeiger	<u>ibid.</u> , p. 256
2888	Role of the Crystal C/A Ratio in Ti_2O_3 and V_2O_3	J. B. Goodenough	<u>ibid.</u> , p. 304
2892	Variational Approach to the Metal Semiconductor Transition	T. A. Kaplan R. A. Bari	<u>ibid.</u> , p. 301
2893	A Raman Study of the Semiconductor-Metal Transition in Ti_2O_3	A. Mooradian P. M. Raccah	<u>ibid.</u> , p. 310
2907	Light Scattering from Hot Electrons in Semiconductors	A. Mooradian A. L. McWhorter	<u>ibid.</u> , p. 380
2915	Acoustoelectric Instabilities in n-GaAs	D. L. Spears	<u>Proceedings National Electronics Conference</u> , Vol. XXVI (NEC, Inc., Oak Brook, Illinois, 1970), p. 342

* * * * *

UNPUBLISHED REPORTS

Journal Articles

<u>JA No.</u>			
3741	Partial and Total Vapor Pressures Over Molten Bi_2Te_3	R. F. Brebrick F. T. J. Smith	Accepted by J. Electrochem. Soc.
3747	Electron Spin Waves in Non-magnetic Conductors: Self-Consistent Field Theory	F. A. Blum	Accepted by Phys. Rev.
3758	Critical Magnetic Properties and Exchange Interactions in EuO	N. Menyuk K. Dwight T. B. Reed	Accepted by Phys. Rev.
3760A	The Liquidus Line and Gibbs Free Energy of Formation of a Crystalline Compound $A_mB_n(c)$. I. The Linear Temperature Approximation	R. F. Brebrick	Accepted by Met. Trans.

Reports

JA No.

3785	A Rapid Scanning Microscope for Light Probing and Infrared Mapping	R. J. Phelan* N. L. DeMeo, Jr.	Accepted by Appl. Optics
3800	Interband Magnetoreflexion of $\text{Hg}_{1-x}\text{Cd}_x\text{Te}$	S. H. Groves T. C. Harman C. R. Pidgeon*	Accepted by Solid State Commun.
3804	Effects of Short Range Interactions on Electron Charge Ordering and Lattice Distortion in the Localized State	R. A. Bari	Accepted by Phys. Rev.
3813	n-p Junction Photovoltaic Detectors in PbTe Produced by Proton Bombardment	J. P. Donnelly T. C. Harman A. G. Foyt	Accepted by Appl. Phys. Letters
3818	A High Temperature Study of Native Defects in ZnTe	F. T. J. Smith	Accepted by J. Phys. Chem. Solids
3826	Raman Spectroscopy of Solids	A. Mooradian	Accepted by <u>Laser Handbook</u> , F. T. Arecchi, Ed. (North-Holland Publishing Co., Amsterdam)
3831	Anomalously High "Mobility" in Semiconductors	C. M. Wolfe G. E. Stillman	Accepted by Appl. Phys. Letters
3840	Anomalous Properties of the Vanadium Oxides	J. B. Goodenough	Accepted by <u>Annual Review of Materials Science</u> , Vol. 1 (Annual Reviews, Inc., Palo Alto)
3842	Light Scattering from Acoustic Plasma Waves and Single-Particle Excitations in Semiconductor Magnetoplasmas	F. A. Blum R. W. Davies	Accepted by Phys. Rev. B
3846	A Relaxation-Time Ansatz for Quantum Transport Theory: Spin Effects	R. W. Davies F. A. Blum	Accepted by Phys. Rev.
3850	Efficient, Single Mode, CW Tunable Spin-Flip Raman Laser	S. R. J. Brueck A. Mooradian	Accepted by Appl. Phys. Letters
3854	Testing Integrated Circuits With a Laser Beam	R. E. McMahon	Accepted by Electronics
3861	Effect of Pressure on the Crystal Structure of CsMnCl_3 and RbMnCl_3	J. M. Longo J. A. Kafalas	Accepted by J. Solid State Chem.

* Author not at Lincoln Laboratory.

<u>MS No.</u>			
2863	Effects of Hydrostatic Pressure and of Jahn-Teller Distortions on the Magnetic Properties of RbFeF_3	J. B. Goodenough N. Menyuk K. Dwight J. A. Kafalas	Accepted by J. de Physique
2961	Effect of Pressure on the Magnetic Properties of $\text{Ca}_{1-x}\text{Sr}_x\text{MnO}_3$	J. A. Kafalas N. Menyuk K. Dwight J. M. Longo	Accepted by J. Appl. Phys.
2966	High Pressure RbFeCl_3 - A Transparent Ferrimagnet	J. M. Longo J. A. Kafalas N. Menyuk K. Dwight	Accepted by J. Appl. Phys.
2992	Varied Roles of the Outer d Electrons	J. B. Goodenough	Accepted by <u>Proceedings of the Robert A. Welch Foundation Conferences on Chemical Research XIV. Solid State Chemistry</u> , Houston, Texas, 9-11 November 1970

Meeting Speeches *

<u>MS No.</u>			
2302A, 2302B	Raman Scattering from Plasmons, Phonons, and Impurities in Semiconductors	G. B. Wright	Seminar, Texas Christian University, 4 January 1971; Colorado State University, 21 January 1971
2899A	Polaron Self-Energy Effects in the Phonon-Assisted Cyclotron Resonance in InSb	E. J. Johnson	Seminar, Naval Research Laboratory, Washington, D. C., 9 December 1970
2915	Acoustoelectric Instabilities in n-GaAs	D. L. Spears	National Electronics Conf., Chicago, Illinois, 7-9 December 1970
2959	Magnetic Properties of Europium: Pressure and Impurity Effects	N. Menyuk K. Dwight J. A. Kafalas	} Sixteenth Annual Conference on Magnetism and Magnetic Materials, Miami Beach, Florida, 16-20 November 1970
2961	Effect of Pressure on the Magnetic Properties of $\text{Ca}_{1-x}\text{Sr}_x\text{MnO}_3$	J. A. Kafalas N. Menyuk K. Dwight J. M. Longo	
2966	High Pressure RbFeCl_3 - A Transparent Ferrimagnet	J. M. Longo J. A. Kafalas N. Menyuk K. Dwight	

*Titles of meeting speeches are listed for information only. No copies are available for distribution.

Reports

MS No.

2970	Canted to Paramagnetic Phase Transition in EuTe	N. F. Oliveira, Jr.* S. Foner* Y. Shapira* T. B. Reed	Sixteenth Annual Conference on Magnetism and Magnetic Materials, Miami Beach, Florida, 16-20 November 1970
2965B	Experiments on Bound Polarons in the Silver Halides	R. C. Brandt	Seminar, University of Utah, 23 November 1970
2986	The Self-Induced Thermal Lens Effect and Related Phenomena in the Atmospheric Propagation of Laser Beams	P. L. Kelley	Ninth Aerospace Sciences Meeting, New York City, 25-27 January 1971
2991	Polaron Magneto-Optics	D. M. Larsen	Greater Washington Solid State Physics Colloquium (GWSSPC), 11 February 1971
2992A	Varied Roles of Outer d Electrons	J. B. Goodenough	Seminar, Catalysis & Surface Material Science Group, Esso Research & Engineering Co., Linden, New Jersey, 11 December 1970
2997	Lattice Effects in the Localized States	R. A. Bari	American Physical Society Meeting, New York, New York, 1-4 February 1971
3009	The Role of the Ambient Gas in Material Preparation and Crystal Growth	T. B. Reed	AIME, Boston Section, Cambridge, Massachusetts, 1 February 1971
3010	Polarization and Linewidth Properties of Broadband Masers	M. M. Litvak	Optics and Infrared Seminar, M.I.T., 2 December 1970
3011	Lattice Effects in Raman Scattering from Semiconductor Plasmas	K. L. Ngai	Physics Seminar, Naval Research Laboratory, Washington, D. C., 16 December 1970
3013	Two Center Excitations in Cr_2O_3 and CoF_2	J. W. Allen	Seminar, Bell Telephone Laboratories, Murray Hill, New Jersey, 9 December 1970
3018	Phase Diagrams and Crystal Growth of Compound and Alloy Semiconductors	J. M. Steininger	Seminars: CNRS, Bellevue, France; LEP, Limeil-Brévannes, France; University of Bordeaux, Talence, France; CENG-LEPI, Grenoble, France; Thomson-CSP Research Center, Orsay, France, 1-28 January 1971
3043, 3043A	Semiconductor-to-Metal Transitions	J. B. Goodenough	Colloquium, Department of Chemistry, Northeastern University, 18 January 1971; Seminar, Electrical Engineering and Chemistry Departments, University of Texas at Austin, 22 January 1971

* Author not at Lincoln Laboratory.

<u>MS No.</u>			
3061A	Multielectron Field Emission	K. L. Ngai	Physics Colloquium, University of Virginia, 3 February 1971
3064	Tunable, CW Infrared Lasers and Their Applications	A. Mooradian	Physics Seminars, National Bureau of Standards, Boulder, Colorado, 14 January 1971
3064A	High Power Tunable CW Infrared Lasers and Their Applications	A. Mooradian	Physics Seminar, Ford Motor Research Laboratories, Dearborn, Michigan, 15 January 1971
3083	Donor Central Cell Corrections in GaAs	D. M. Larsen	Physics Colloquium, Naval Research Laboratory, 11 February 1971
3091	Optical Properties of the Alkalis Using the KKR-Z Method	C - Y. Young	Physics Seminar, City University of New York, 16 February 1971

ORGANIZATION

SOLID STATE DIVISION

A. L. McWhorter, *Head*
P. E. Tannenwald, *Associate Head*
C. R. Grant, *Assistant*

OPTICAL AND ELECTRONIC PHYSICS

H. J. Zeiger, *Leader*
A. Mooradian, *Associate Leader*
P. L. Kelley, *Assistant Leader*

Bari, R. A.	Larsen, D. M.
Brodersen, R. W.*	Ngai, K. L.
Brueck, S.*	Palm, B. J.†
Davies, R. W.	Pine, A. S.
Dresselhaus, G. F.	Rossi, J. A.
Johnson, E. J.	Young, C-Y.
Landon, S. N.	

SOLID STATE PHYSICS

J. G. Mavroides, *Leader*
G. B. Wright, *Assistant Leader*

Allen, J. W.	Fetterman II.
Barch, W. E.	Groves, S. II. (LOA)
Blum, F. A., Jr.	Henrich, V. E.
Burke, J. W.	Kernan, W. C.
Chinn, S. R.	Kolesar, D. F.
DeFeo, W. E.	Melngailis, J.
Dresselhaus, M. S.†	Menyuk, N.
Dwight, K., Jr.	Nil, K. W.
Feldman, B.	Parker, C. D.

ELECTRONIC MATERIALS

J. B. Goodenough, *Leader*
A. J. Strauss, *Associate Leader*

Anderson, C. II., Jr.	Mastromattei, E. L.
Banus, M. D.	Mroczkowski, I. II.
Batson, D. A.	Owens, E. B.
Button, M. J.	Pantano, J. W.
Delaney, E. J.	Pierce, J. W.
England, R. F.	Plonko, M. C.
Fahey, R. E.	Raccab, P. M.
Finn, M. C.	Reed, T. B.
Iseler, G. W.	Stack, T. E.
Kafalas, J. A.	Steininger, J. M.
LaFleur, W. J.	Temkin, R. J.*
Lavine, M. C.†	Tracy, D. M.

APPLIED PHYSICS

J. O. Dimmock, *Leader*
T. C. Harman, *Assistant Leader*
I. Melngailis, *Assistant Leader*

Belanger, L. J.	Lindley, W. T.
Calawa, A. R.	Murphy, R. A.*
Carter, F. B.	Orphanos, W. G.
DeMeo, N.	Paladino, A. E.
Donnelly, J. P.	Spears, D. L.
Elliott, C. T.‡	Stillman, G. E.
Ferrante, G. A.	Ward, J. H. R., III
Foyt, A. G.	Wolfe, C. M.
Hancock, R.	Woods, R. J.
Hurwitz, C. E.	Youtz, P.
Krohn, L., Jr.	

MICROELECTRONICS

R. E. McMahon, *Leader*

Bachner, F. J.	Gray, R. V.
Beatrice, P. A.	McBride, W. F.
Childs, N. B.	McGonagle, W. H.
Clough, T. F.	Mountain, R. W.
Cohen, R. A.	Pichler, H. H.
Durant, G. L.	Pybus, V. J.
Grant, L. L.	Wilde, R. E.

MICROSOUND

E. Stern, *Leader*

Alusow, J. A.	Smith, H. I.
Brogan, W. T.	Waldron, R. A.
Burke, B. E.	Williamson, R.
Chen, F.	

* Research Assistant

† Part Time

‡ Visiting Scientist

I. SOLID STATE DEVICE RESEARCH

A. N-P JUNCTION PHOTOVOLTAIC DIODES IN PbTe AND $\text{Pb}_{1-x}\text{Sn}_x\text{Te}$ PRODUCED BY PROTON BOMBARDMENT

We have previously reported that proton bombardment can be used to convert p-type PbTe into n-type material and that this technique can be used to fabricate n-p junction photovoltaic diodes in PbTe (Ref. 1). In this section, we will describe our progress in fabricating PbTe diodes and report the extension of this fabrication method to $\text{Pb}_{1-x}\text{Sn}_x\text{Te}$.

1. PbTe

The PbTe substrates were p-type Bridgman grown single crystals which had 77°K carrier concentrations of $7 \times 10^{18}/\text{cm}^3$ and hole mobilities of $10,000 \text{ cm}^2/\text{V}\cdot\text{sec}$. Photovoltaic detectors were prepared using the method described in Ref. 1 in two geometric configurations: (a) 5-mil-diameter diodes with a 3-mil-diameter concentric Au contact and (b) 15-mil-square diodes with a 5-mil-diameter Au contact. In both of these configurations, a broad area Au ohmic contact was electroplated on the back of each sample to serve as a contact to the p-type material. At 77°K the best 5-mil-diameter PbTe diode had a zero-bias resistance of $2.4 \text{ M}\Omega$ for a resistance-area product of $300 \Omega\text{-cm}^2$, while the best 15-mil-square diode had a resistance of $190 \text{ k}\Omega$ for a resistance-area product of $280 \Omega\text{-cm}^2$.

Blackbody detectivity and relative response measurements were carried out with the PbTe diodes at 77°K, using a 500°K blackbody and chopping frequencies between 100 and 800 Hz. With an 80° field of view, 295°K background, the best 5-mil-diameter diode has a peak detectivity of $1.5 \times 10^{11} \text{ cmHz}^{1/2}/\text{W}$ and a peak quantum efficiency of 36 percent at $5 \mu\text{m}$. For the 15-mil-square diode, the peak detectivity is $1.4 \times 10^{11} \text{ cmHz}^{1/2}/\text{W}$ and the quantum efficiency 32 percent.

When the background was reduced by use of a cooled f/6 aperture, the noise voltage decreased by over a factor of two on both diodes, resulting in an increase in the peak detectivity to $3.4 \times 10^{11} \text{ cmHz}^{1/2}/\text{W}$ for the 5-mil diode and $3.2 \times 10^{11} \text{ cmHz}^{1/2}/\text{W}$ for the 15-mil-square diode. Under these conditions, the noise voltage is consistent with the calculated Johnson noise for these devices. The reduced background detectivity of the 5-mil diode as a function of wavelength is shown in Fig. I-1.

Capacitance voltage measurements indicate that these junctions are essentially linearly graded, with $C \sim (V + V_D)^{-1/2}$.⁹ The effective carrier concentration at the edge of the depletion layer is approximately $5 \times 10^{17}/\text{cm}^3$ with a gradient of $3 \times 10^{22}/\text{cm}^4$.

To study the annealing characteristics of the bombarded layer, 5-mil-diameter diodes were prepared as in Ref. 1, except that Pt instead of Au was used as the contact on the bombarded layer and the substrate. Using 1-hour anneals, no change was observed for anneal temperatures up to 110°C. At 125°C, however, the zero-bias resistance decreased by 25 percent and the capacitance increased by 10 percent.

2. $\text{Pb}_{1-x}\text{Sn}_x\text{Te}$

P-n junction photovoltaic diodes have also been fabricated in $\text{Pb}_{0.88}\text{Sn}_{0.12}\text{Te}$ using this technique. The p-type substrates were Bridgman-grown single crystals which had 77°K carrier concentrations of approximately $8 \times 10^{17}/\text{cm}^2$ and hole mobilities of $13,000 \text{ cm}^2/\text{V-sec}$. At 77°K, resistance-area products as high as $0.36 \Omega\text{-cm}^2$ were observed for both 5-mil circular ($2.8 \text{ k}\Omega$) and 15-mil-square (250Ω) mounted diodes. It should be noted, however, that several unmounted diodes exhibited values two to three times higher, indicating that our present mounting techniques may be degrading these diodes, and that by improving our bonding techniques, we can improve on the detectivities reported below.

Peak detectivities, D_λ^* ($7 \mu\text{m}$, 500, 1) as high as $1.2 \times 10^{10} \text{ cmHz}^{1/2}/\text{W}$ with a quantum efficiency of 27 percent at $7 \mu\text{m}$ were observed at 77°K. The detectivity of these diodes as a function of wavelength is shown in Fig. I-1.

Capacitance-voltage measurements on these diodes indicate that the diodes are nearly abrupt junctions, with $C \sim (V + V_D)^{-1/2}$. This difference between our PbTe and $\text{Pb}_{0.88}\text{Sn}_{0.12}\text{Te}$ diodes is probably due to the lower substrate carrier concentration in $\text{Pb}_{0.88}\text{Sn}_{0.12}\text{Te}$.

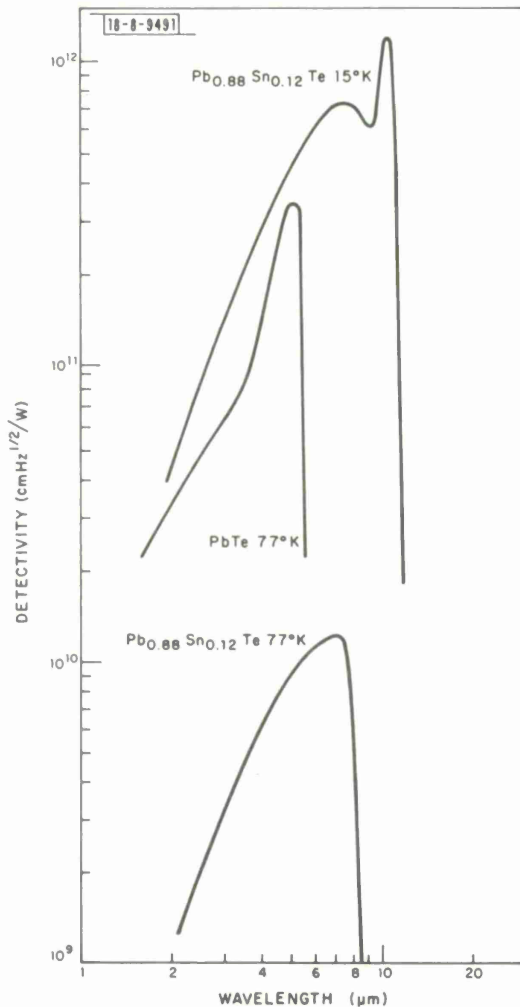


Fig. I-1. Reduced background detectivity of PbTe and $\text{Pb}_{0.88}\text{Sn}_{0.12}\text{Te}$ diodes as a function of wavelength.

At 15°K, the best 15-mil-square diode had a zero-bias resistance of 667 k Ω and a resistance-area product of 966 Ω -cm². All the 5-mil circular diodes tested to date exhibited additional leakage current at low temperatures. For the 15-mil diode, the zero-bias RC time constant is 2.5 msec (667 k Ω \times 3800 pf), with a 3-dB rolloff frequency of 63 Hz.

The 500°K blackbody responsivity of this diode was measured as a function of frequency with an $f/2$, $f/6$ and $f/8$, 295°K background and found to be essentially independent of the aperture. The relative spectral responsivity was measured with an $f/2$, 295°K background. The peak detectivities obtained from these measurements and measurements of the total system noise as a function of frequency and background are plotted in Fig. I-2. For this diode the peak detectivity occurs at 10.2 μ m with a peak quantum efficiency of 37 percent.

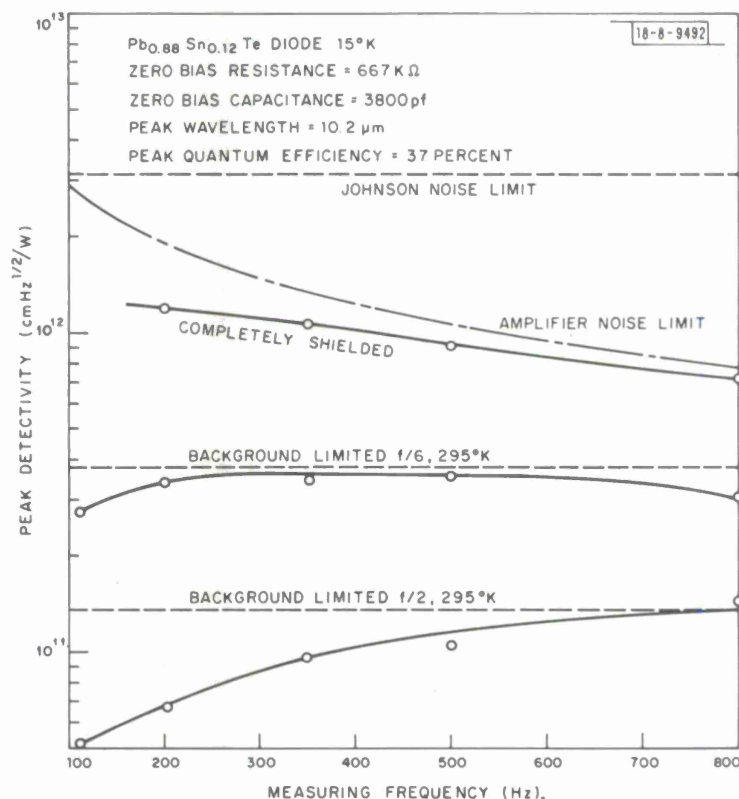


Fig. I-2. Peak detectivity ($\lambda = 10.2 \mu\text{m}$) of 15-mil-square $\text{Pb}_{0.88}\text{Sn}_{0.12}\text{Te}$ diode at 15°K as a function of frequency and background.

With a large field of view ($f/2$ system), the detectivity increases with frequency, indicating that the diode is exhibiting $1/f$ noise. With an $f/6$ shield, although there still appears to be some $1/f$ noise at lower frequencies, the detectivity is flatter as a function of frequency. At the higher frequencies the amplifier noise becomes important due to the RC rolloff in both the responsivity and diode noise. With the diode completely shielded, the peak detectivity calculated at 200 Hz and below is greater than 10^{12} cmHz^{1/2}/W. At 800 Hz, the system is amplifier noise limited, but at lower frequencies, the system is neither amplifier noise limited nor Johnson noise limited, indicating that there is excess noise. The source of the excess noise is not yet understood.

Section I

TABLE I-1 SUMMARY OF RESULTS OBTAINED TO DATE ON PbTe AND $\text{Pb}_{0.88}\text{Sn}_{0.12}\text{Te}$				
Material	Temperature	Peak Wavelength (μm)	Peak Quantum Efficiency (percent)	Reduced Background $D_{\lambda}^*(\lambda, 200, 1)$ ($\text{cmHz}^{1/2}/\text{W}$)
PbTe	77°K	5	36	3.4×10^{11}
$\text{Pb}_{0.88}\text{Sn}_{0.12}\text{Te}$	77°K	7	27	1.2×10^{10}
$\text{Pb}_{0.88}\text{Sn}_{0.12}\text{Te}$	15°K	10.2	37	1.2×10^{12}

The detectivity calculated for the completely shielded situation is shown in Fig. I-1 as a function of wavelength. Although the dip in detectivity around $9\mu\text{m}$ is not completely understood, similar dips have been observed in diffused $\text{Pb}_{1-x}\text{Sn}_x\text{Te}$ diodes.² Table I-1 summarizes the best results obtained to date on PbTe and $\text{Pb}_{0.88}\text{Sn}_{0.12}\text{Te}$.

J. P. Donnelly
T. C. Harman
A. G. Foyt

B. CONTINUOUS-WAVE $\text{Pb}_{0.93}\text{Sn}_{0.07}\text{Te}$ DIODE LASERS AT $8.6\mu\text{m}$

Diode lasers which at 4.2°K emit continuous $8.6\text{-}\mu\text{m}$ radiation have been fabricated for use in high resolution spectroscopy of pollutant gases. Continuous output powers up to $40\mu\text{W}$ and pulsed powers up to 10mW have been obtained. The diodes were fabricated from crystals which were vapor grown from a thallium-doped source.

The thallium doping enabled us to use essentially the same processes to fabricate diode lasers at $8.6\mu\text{m}$ from $\text{Pb}_{0.93}\text{Sn}_{0.07}\text{Te}$ as were successful in producing diode lasers at $10.6\mu\text{m}$ from $\text{Pb}_{0.88}\text{Sn}_{0.12}\text{Te}$. The crystals are vapor grown at a temperature of approximately 800°C from a metal-rich ingot. For $\text{Pb}_{1-x}\text{Sn}_x\text{Te}$ in the approximate composition range $0.08 < x < 0.2$, this produces crystals with p-type extrinsic bulk conductivity and an n-skin which is formed on air cooling without doping.³ For $x < 0.08$, crystals grown by the same process are n-type throughout the bulk because they either are n-type at the growth temperature or they convert to n-type upon cooling. The effect is due to a shift in the solidus field which occurs when the alloy composition is changed. For compositions of $\text{Pb}_{1-x}\text{Sn}_x\text{Te}$ with $x \leq 0.32$, our experimental results show that there is a metal saturation temperature, T_i , above which metal-saturated crystals have an extrinsic p-type carrier concentration. Crystals metal-saturated at temperatures below T_i are n-type. These results assume that saturation equilibrium is reached at the saturation temperature and is maintained in the bulk when the crystal is cooled. Approximate values of T_i are plotted in Fig. I-3 as a function of the mole fraction of SnTe in the alloy. Forming the

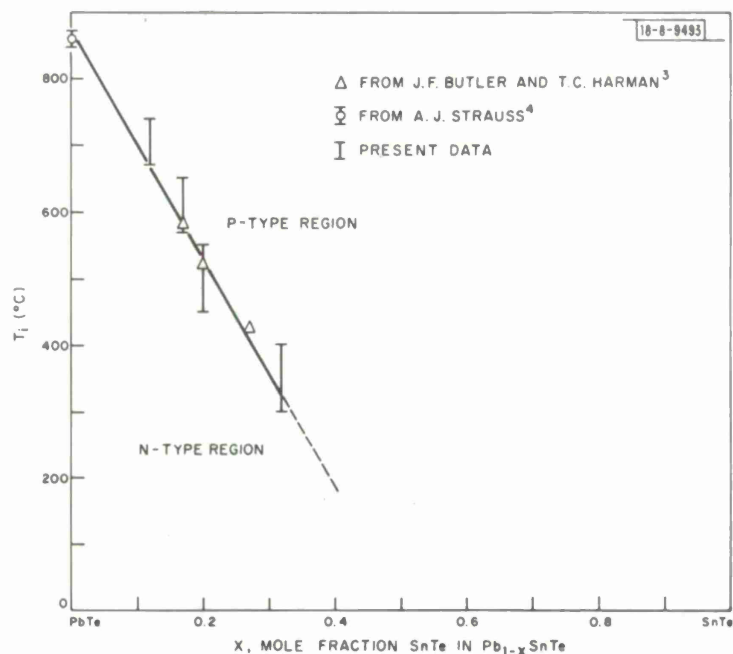


Fig. I-3. P-n crossover temperature T_i versus mole fraction SnTe for metal-saturated $Pb_{1-x}Sn_xTe$.

p-n junction during the cooling cycle is attractive because it eliminates the need for additional processing steps in which contamination could result. In order to extend this technique to alloys with $x < 0.08$, we have doped the vapor-grown crystals with thallium, which is a p-type impurity in $Pb_{1-x}Sn_xTe$ and therefore serves to compensate the donors produced by excess-metal stoichiometric defects. In effect, the thallium reduces the temperature T_i in Fig. I-3 such that the 800°C growth temperature is sufficiently above the p-n crossover temperature, where p-type crystals grow. An n-skin is then diffused into the crystals during cooling.

Several crystals of $Pb_{0.93}Sn_{0.07}Te$ were grown from the vapor phase by two techniques: a closed tube vertical process and a closed tube horizontal process described below. In each case the vapor source consists of a metal-rich, two-phase ingot of $(Pb_{0.93}Sn_{0.07})_{1-y}Te_y$, with $y < 0.5$. Using a crystal growth temperature of approximately 800°C, the as-grown and air cooled crystals were n-type throughout at room temperature. By adding 6.2 mg of thallium selenide to each 100-g charge of the metal-rich source material for the vertical process, and 12.3 mg of pure thallium to a similar quantity of the source material for the horizontal growth process, it is possible to grow crystals having p-type bulk conductivity with an n-type skin which is formed on cooling.

A. R. Calawa
T. C. Harman

C. CLOSED-TUBE HORIZONTAL VAPOR GROWTH OF $Pb_{1-x}Sn_xTe$ CRYSTALS

$Pb_{1-x}Sn_xTe$ crystals have been grown by a horizontal closed-tube vapor transport process. The essential difference between this process and the vertical growth procedure³ is that the

Section I

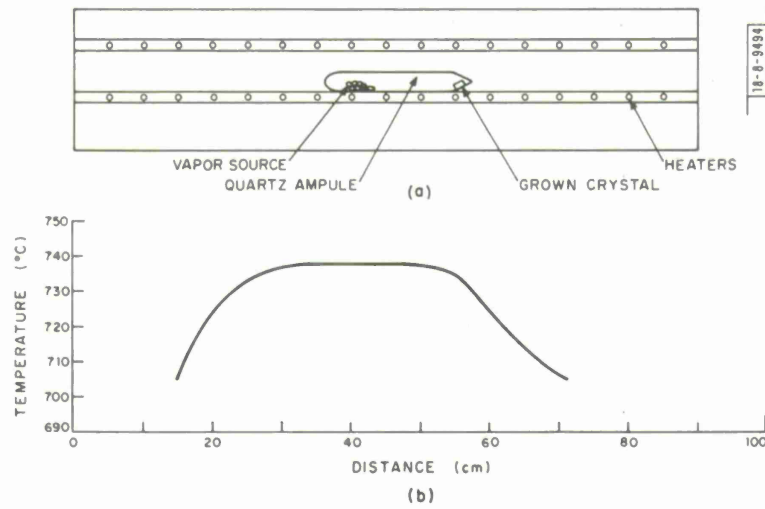


Fig. 1-4. (a) Schematic diagram of closed-tube horizontal crystal growth apparatus for $Pb_{1-x}Sn_xTe$. (b) Temperature profile for growing crystals by closed-tube horizontal growth technique.

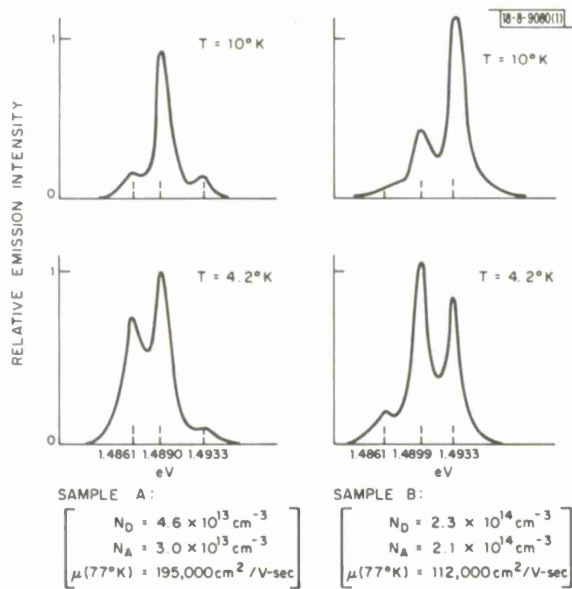


Fig. 1-5. Pertinent photoluminescence spectra from two GaAs epitaxial layers. Bottom two traces were taken with each sample at $4.2^\circ K$, upper two at $10^\circ K$.

transport is greatly enhanced by convection currents of the $\text{Pb}_{1-x}\text{Sn}_x\text{Te}$ vapor within the closed tube.

The tube arrangement and typical temperature profile are shown in Fig. I-4. To obtain the vapor source, a 100-g charge of the elements mixed in the proportion $(\text{Pb}_{1-x}\text{Sn}_x)_{0.501}\text{Te}_{0.499}$ is heated isothermally at 1050°C for two hours and water quenched. This ingot is crushed to a powder and thoroughly mixed. A 5-g charge of the powder is used as the source. The growth ampoule is a quartz tube 25 mm in diameter and 20 to 25 cm long. The growth end of the tube is formed in the shape of a cone and fire polished. The ampoule containing the source powder is evacuated and sealed at a pressure $<2 \times 10^{-6}$ mmHg. The source end of the ampoule is placed in an isothermal zone set at 740°C . The cone end of the ampoule is set in a temperature gradient of $2.5^\circ\text{C}/\text{cm}$ with the tip of the cone set at 730°C . Under these conditions, a single nucleation usually occurs on the tapered part of the cone. The transport rate is approximately 5 mg/hour, and growth times range from 16 to 64 hours. The crystals have well-defined $\langle 100 \rangle$ and $\langle 111 \rangle$ facets, and the $\langle 100 \rangle$ planes have surface areas of 4 mm^2 to 1 cm^2 .

A. R. Calawa
R. Woods
T. C. Harman

D. ACCEPTOR LUMINESCENCE IN HIGH PURITY n-TYPE GaAs

We have examined the acceptor luminescence in two dozen high purity n-type GaAs samples with impurity concentrations in the range $7 \times 10^{13} \text{ cm}^{-3} \leq N_D + N_A \leq 5 \times 10^{15} \text{ cm}^{-3}$. All samples used were grown in an effort to obtain high purity GaAs. The donors and acceptors present are therefore residual and not intentionally introduced dopants. Consequently, no correlation of the acceptor photoluminescence spectra with the presence or absence of specific chemical impurities will be attempted here. The samples discussed here were selected because they accurately represent the different photoluminescence spectra observed by previous workers⁵⁻¹² and by us in samples with low total electrically active impurity content. All the samples are n-type; the values of N_D and N_A for each sample (cf. Fig. I-5) are calculated from Ref. 13.

We show as the bottom two traces in Fig. I-5 typical photoluminescence spectra obtained from two different samples at 4.2°K with no applied magnetic field. For simplicity we have omitted the near-edge emission (at higher energies) and phonon replicas (at lower energies) since they are not germane to the discussion presented here. Note that each sample is dominated by a pair of luminescence peaks (the position in energy of each peak is given in Fig. I-5). The samples appear to have the 1.4861- and 1.4933-eV transitions in common. Spectra similar to the left curve (sample A) have been reported in Refs. 5, 7 and 11, and spectra similar to the right trace (sample B) have been reported in Refs. 6, 8, 9 and 10.

The upper traces in Fig. I-5 show the effect of increasing temperature on the sample luminescence. Each sample has one peak which rapidly grows in intensity (A: 1.4890 eV and B: 1.4933 eV) and one which rapidly falls (A: 1.4861 eV and B: 1.4899 eV). Temperature effects similar to these have been reported in every GaAs photoluminescence article in which the peaks were observable and the temperature was varied.^{6-10, 12} Although we do not consider the temperature data conclusive, they suggest that similar recombination mechanisms are operative in both crystals but at slightly different energies.

Section I

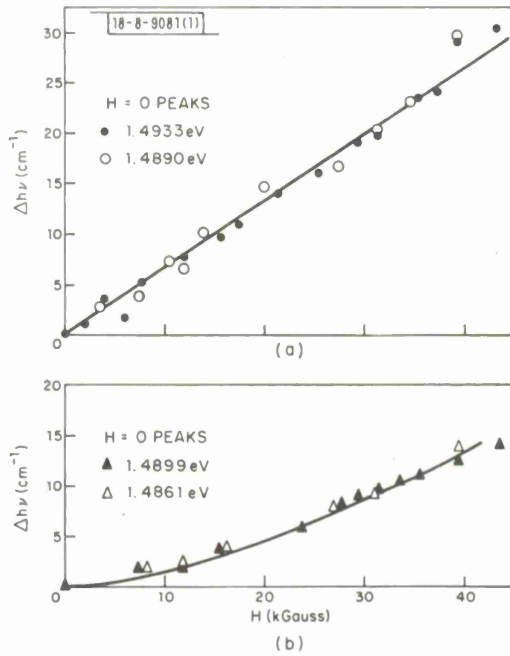


Fig. I-6. (a) Behavior of the 1.4933- and 1.4890-eV peaks in a magnetic field. Both peaks move linearly in H. (b) Shifts of 1.4861- and 1.4899-eV transitions in H are shown. As in Fig. I-6(a), both transitions move at same rate.

Figure I-6 shows the effects of a magnetic field on the various recombination peaks. In Fig. I-6(a) the shift in the peak position of the 1.4933- (solid circles) and 1.4890-eV (open circles) transitions are plotted against magnetic field. Note that both transitions move linearly in H to higher energy, and both do so at the same rate. In Fig. I-6(b) the shifts in the peak positions of the 1.4899- (solid triangles) and 1.4861-eV (open triangles) transitions are plotted against H. These shifts are roughly quadratic in H, and again the rates of shift for each are the same. We resolve no splitting of these lines in fields $\lesssim 40$ kG which is consistent with small g-factors for electrons and holes.¹⁴ The solid line in Fig. I-6(a) will be discussed below.

Considering a free electron - neutral acceptor transition, (e, A^0) , in zero magnetic field we have

$$h\nu(e, A^0) \approx E_c - E_A \quad (1)$$

where E_c is the bottom of the conduction band and E_A is the acceptor energy level. As is well known, in a magnetic field the conduction band is broken into several magnetic sub-bands. Considering only the bottom-most level ($n = 0$), in a magnetic field the recombination peak will now be at

$$h\nu(e, A^0; H) = E_c - E_A + \frac{e\hbar H}{2m^*c} - \Delta E_A(H) \quad (2)$$

The shift in energy is given by the difference between expressions (1) and (2). The straight line in Fig. I-6(a) is drawn with slope $e\hbar/2m^*c$, with $m^* = 0.072 m_0$. The slight discrepancy from the measured value¹⁵ of electron mass at the bottom of the band of $0.0665 m_0$ is probably due to a band filling effect which is larger at low magnetic fields and decreases at large fields due to

the increase in the density of states at the bottom of the band. This results in a reduction of the slope $\Delta h\nu$ versus H and an increase in calculated value of m^* . Except for this effect, the excellent fit to the data by a straight-line dependence confirms the identification of both the 1.4933- and 1.4890-eV transitions as free electron - neutral acceptor. Considering the depth of the binding energies for the two acceptors (~ 27 and 31 meV), we expect $\Delta E_A(H)$ to be small, $\sim 0.2 \text{ cm}^{-1}$ at 40 kG. At higher fields we would expect E_A to shift, leading to an even faster increase in $h\nu(e, A^0; H)$.

The temperature data (cf. Fig. I-5 and Refs. 6, 7, 9 and 10) further support this assignment. As shown in Fig. I-5, both the 1.4933-eV and 1.4890-eV transitions gain in intensity as the temperature is increased. This is quite consistent with an increase in the concentration of free electrons as seen in the Hall measurements for these same samples (thermal ionization of shallow donors).¹⁶ Application of a small d. c. bias (~ 1 V), sufficient to impact ionize the shallow donors, also greatly enhances the (e, A^0) transitions.

We now discuss the recombination peaks at 1.4861 and 1.4899 eV. First, we note that the transitions always occur in these pairs: (1.4861, 1.4890) and (1.4899, 1.4933). In every published article dealing with GaAs of low total electrically active impurity concentration (Refs. 5-12) pairs of lines in this spectral range have been observed. Earlier proposed assignments of the 1.4861- and 1.4899-eV lines associated with the (e, A^0) 1.4890- and 1.4933-eV lines, respectively, include the phonon sideband model,^{5, 11} exciton ionized-acceptor (X, A^-) recombination,⁶⁻¹⁰ and donor-acceptor pair recombination.^{6-10, 12} The magnetic field data rule out the phonon sideband model, since the lines do not shift linearly in a magnetic field.

The photoluminescence of these two bands under varying light intensity clearly displays the characteristics of donor-acceptor pair recombination. In Fig. I-7 we plot the separation in energy between the peak positions of each associated pair (that is, $h\nu_{1.4933} - h\nu_{1.4899}$ and $h\nu_{1.4890} - h\nu_{1.4861}$) as a function of incident light intensity. The higher energy pair are plotted as solid triangles and the lower energy pair as open triangles. For reference, all the data in Figs. I-5 and I-6 were taken at $I/I_0 = 1$. As the incident intensity is decreased, 1.4933- and 1.4890-eV transitions remain essentially fixed in energy so that the data in Fig. I-7 reflect only the shift

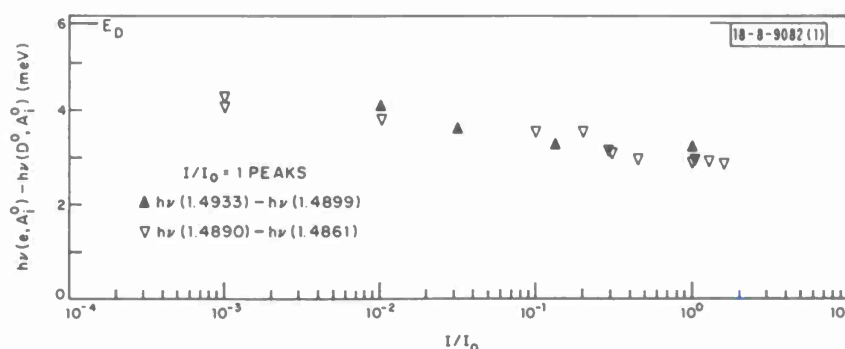


Fig. I-7. Solid triangles are separation in energy (meV) between 1.4933- and 1.4899-eV transitions as I/I_0 is varied. Open triangles represent same data for pair 1.4890 and 1.4861 eV. As I/I_0 is decreased, 1.4899- and 1.4861-eV transitions shift to lower energies causing increase in separation. Data in Figs. I-5 and I-6 were taken at $I/I_0 = 1$.

Section I

of associated lower energy bands to longer wavelength. The data show that as I/I_0 is decreased the energy difference between the peaks increases, reaching ~ 4.3 meV at $I/I_0 \approx 10^{-3}$. Lower intensity measurements have not been possible. The energy of donor-acceptor pair recombination is given approximately by

$$h\nu(D^0, A^0) = E_D - E_A + e^2/\kappa R_{DA} \quad (3)$$

where κ is the dielectric constant and R_{DA} is the distance between the donor acceptor pair. As discussed by Thomas,¹⁷ at low excitation intensity recombination involving distant pairs is more probable and the coulomb term $e^2/\kappa R_{DA}$ is less significant. As the intensity increases, the more distant pairs saturate and the recombination peak moves to higher energies.

The temperature behavior of these peaks is also consistent with (D^0, A^0) recombination. The intensity of both peaks decreases as the temperature increases, again consistent with thermal ionization of neutral donors.¹⁶ A small electric field produces the same effect.

The magnetic field data for these transitions [Fig. I-6(b)] show a rather large shift, ~ 14 cm⁻¹ in 40 kG. Using the results of Larsen¹⁸ we have calculated the shift in the ground state energy of a donor to be only ~ 7 cm⁻¹ in 40 kG. Since we have previously established $\Delta E_A(H) \approx 0$, the difference between these numbers must be due to a change in term $e^2/\kappa R_{DA}$ in Eq. (3) due to a shift in the recombination from more remote to more closely spaced pairs induced by the magnetic field. This is not unexpected since as the magnetic field is increased the size of the (donor) electron orbit shrinks, favoring recombination of more closely spaced pairs. Although an exact quantitative prediction of this effect is difficult to calculate, the following argument does yield a rough estimate of the magnitude involved. At zero magnetic field, the magnitude of the coulomb interaction term may be used to estimate $\langle R_{DA} \rangle \sim 400 \text{ \AA}$. The additional shift of ~ 7 cm⁻¹ then corresponds to a change of $\langle R_{DA} \rangle$ to $\sim 310 \text{ \AA}$. This is consistent with the calculated donor wave function contraction in a field of 40 kG (Ref. 18).

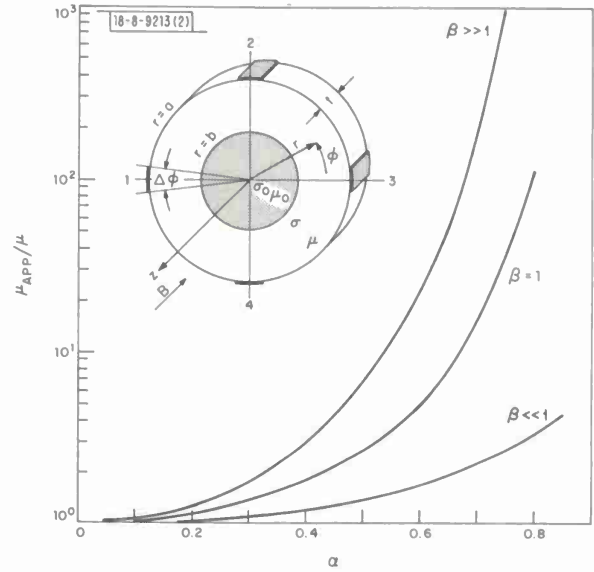
J. A. Rossi J. O. Dimmock
C. M. Wolfe G. E. Stillman

E. ANOMALOUSLY HIGH "MOBILITY" IN SEMICONDUCTORS

The effects of various types of inhomogeneity on the measured mobility of semiconductors have been examined theoretically in some detail.¹⁹ All these treatments have shown that the measured mobility of inhomogeneous samples should be anomalously low either as a result of the averaging inherent to the Hall constant and resistivity measurements or as a result of carrier scattering. Although anomalously low mobilities are commonly observed experimentally,²⁰ anomalously high mobilities have been observed in silicon where an accumulation layer was induced on a high-resistance n-type sample by an HF treatment²¹ and in GaAs which was grown under metal-rich conditions.²² Mobilities which appear to be anomalously high have also been reported for (PbSn) Te (Ref. 23). We have developed a simple model for an inhomogeneous semiconductor which leads to an anomalously high measured mobility and which qualitatively accounts for some of these experimental observations.

The model which is used to demonstrate that an anomalously high apparent mobility can be obtained in an inhomogeneous semiconductor is shown in Fig. I-8. Van der Pauw's method²⁴ is

Fig. I-8. Ratio of apparent mobility, μ_{APP} , to real mobility, μ , as a function of relative extent of inhomogeneity, $\alpha \equiv b/a$, for several values of $\beta \equiv \mu B$. Analysis of resistivity and Hall constant measurements with $\sigma_o \gg \sigma$ leads to an anomalously high apparent mobility as indicated by curves. Inset shows cylindrically symmetric van der Pauw configuration, $r = a$, with conducting inhomogeneity, $r = b$, which was used for analysis.



used to determine values of resistivity, ρ , and Hall constant, R_H , for this sample with a cylindrical inhomogeneity in the center. The conductivity, σ , and the mobility, μ , are assumed to be discontinuous at the boundary between the two regions, and the conductivity of the inhomogeneity, σ_o , is assumed to be much greater than the conductivity of the medium, σ .

To obtain the apparent resistivity from the van der Pauw measurement, we pass a current through the contacts at 1 and 2 and determine the voltage induced between the contacts at 3 and 4. Using van der Pauw's equation and the expression for the potential, the apparent resistivity, ρ_{APP} , is given by

$$\rho_{APP} = \frac{\pi}{\ln 2} \frac{V_{34}t}{I_{12}} = \frac{1}{\sigma \ln 2} \sum_{n=1}^{\infty} \frac{(1 - \alpha^{2n})^3}{(1 + \alpha^{4n})(1 + \alpha^{2n})} \frac{(-1)^{n+1}}{n}, \quad (4)$$

where $\alpha \equiv b/a$.

To obtain the apparent Hall constant, we pass a current through the contacts at 1 and 3 with a magnetic field in the z-direction and determine the voltage induced between the contacts at 2 and 4. The apparent Hall constant, $(R_H)_{APP}$, is given by

$$(R_H)_{APP} = \frac{V_{24}t}{I_{13}B} = \frac{4}{\pi} \frac{\mu}{\sigma} \sum_{n=1}^{\infty} \frac{(1 + \beta)^2}{\left(\frac{1 + \alpha^{4n-2}}{1 - \alpha^{4n-2}}\right)^2 + \beta^2} \frac{(-1)^{n+1}}{(2n-1)}, \quad (5)$$

where $\beta \equiv \mu B$. The apparent mobility is then

$$\mu_{APP} = (R_H)_{APP} / \rho_{APP} \quad (6)$$

From Eqs. (4) and (5) we can examine the effect of the conducting inhomogeneity on the values of resistivity and Hall constant. In the absence of an inhomogeneity, $\alpha = 0$, the series in Eq. (4) reduces to $\ln 2$ so that $\rho_{APP} = 1/\sigma = \rho$. The series in Eq. (5) reduces to $\pi/4$ and $(R_H)_{APP} = \mu/\sigma = R_H$ so that the apparent mobility is then equal to the true mobility of the sample. In the low field

Section I

limit, $\beta \ll 1$, as the size of the inhomogeneity increases, $\alpha > 0$, both the resistivity and Hall constant decrease. However, the resistivity decreases faster than the Hall constant, thus giving a higher apparent mobility. Physically, this is a geometrical effect where the current lines in the Hall constant measurement tend to spread around the inhomogeneity more than the current lines in the resistivity measurement. Thus, the Hall voltage is affected less than the resistivity voltage by the shunting effect of the conducting inhomogeneity.

As the magnetic field increases for a given size inhomogeneity, the Hall constant increases and, since the resistivity remains constant, the apparent mobility increases. In the high field limit, $\beta \gg 1$, the measured Hall constant is equal to μ/σ which is the Hall constant of a homogeneous sample. Physically, this effect is a result of the current lines being distorted out of the inhomogeneity until in the high field limit there is no current flow into the inhomogeneity. As has been pointed out previously,²⁵ this is a consequence of the boundary conditions between the inhomogeneity and the surrounding medium.

These results are summarized quantitatively in Fig. I-8 where the ratio of the apparent mobility to the true mobility is plotted as a function of the relative size of the inhomogeneity, α , for several values of $\beta \equiv \mu B$. As can be seen, the apparent mobility can be several orders of magnitude higher than the real mobility, depending upon the size of the conducting inhomogeneity and the value of β .

To obtain an experimental verification of this simple model, conducting inhomogeneities were intentionally introduced into thin epitaxial layers of GaAs which were grown on semi-insulating substrates. Conducting n^+ regions were produced by alloying tin, and metallic inclusions were simulated by alloying gallium into the upper surface of a number of samples. To test the generality of the model, a number of commonly used van der Pauw configurations were examined, including cloverleaves, crosses, squares, and circles, and in all configurations the apparent mobility could be substantially increased by the introduction of a conducting inhomogeneity. This effect was also observed in the standard rectangular Hall geometry. By intentionally introducing conducting inhomogeneities, we have increased the apparent 300°K mobility from 7400 to 24,000 $\text{cm}^2/\text{V-sec}$ and the apparent 77°K mobility from 150,000 to 740,000 $\text{cm}^2/\text{V-sec}$ in qualitative agreement with the simple model.

These results cast some doubt on the use of high mobility values alone as an indication of the quality of a material, unless the homogeneity can be established. Perhaps the easiest method of determining the homogeneity of the material is to examine the magnetic field dependence of the Hall constant. Since this type of inhomogeneity leads to an increase in Hall constant with β , as shown in Fig. I-8, if the Hall constant is observed to decrease with the expected decrease in the Hall coefficient factor, then inhomogeneity effects of this type can probably be considered negligible.

C. M. Wolfe
G. E. Stillman

F. EFFICIENT, SINGLE MODE, CW, TUNABLE SPIN-FLIP RAMAN LASER

We report the efficient operation of a CW spin-flip Raman laser in InSb, using a CO laser as a pump. A previous report²⁶ on the CW spin-flip Raman laser indicated operation in a total internal bounce mode with efficiencies of about 1 percent. In the present results we have achieved conversion efficiencies in excess of 50 percent with the incident and Raman beams collinear. The

Raman laser operated in both single axial and single transverse mode. Axial mode hopping and pulling were observed as a function of magnetic field.

The experimental arrangement was discussed in a previous publication.²⁶ A carbon monoxide laser operating with a single line output of a few watts was used to resonantly excite the InSb crystals. InSb samples with electron concentrations in the range of 1 to $3 \times 10^{16} \text{ cm}^{-3}$ were cut in the shape of parallelepipeds having lengths between two flat and parallel faces of several millimeters. The samples were conduction cooled in the bore of a superconducting solenoid. Actual sample temperatures, however, in the active region were probably much higher than 4.2°K at the highest pump intensities. The high resolution data were recorded using a double grating spectrometer having a spectral width of less than 0.1 cm^{-1} . The incident laser and Raman laser beams propagated normal to the direction of the magnetic field, \underline{H} . In order to minimize sample heating at the highest pump intensities, the incident laser beam was chopped at a 6 percent duty cycle.

With the Raman laser operating in a collinear geometry, the Raman laser output beam was polarized perpendicular to the magnetic field when the pump beam was polarized parallel to the magnetic field. This observation is consistent with theoretically predicted selection rules.^{27,28}

The overall power conversion efficiency is defined here to be $\eta = P_R/P_L$, where P_R is the Raman laser output from both ends of the crystal and P_L is the pump laser power incident on the front face of the crystal. We have observed efficiencies in excess of 50 percent and output powers in excess of one watt with only the natural 36-percent reflectivity faces on the sample. If one allows for the power reflected from the front face of the crystal, the ratio of P_R to the laser power which gets into the crystal is in excess of 75 percent. The spin saturation discussed by Patel²⁹ for CO_2 laser excitation does not occur in the present case because of the lower power densities necessary to achieve high conversion efficiencies.

Thresholds of less than 50 mW of TEM_{00} pump laser power in an estimated 50- to 100- μm focal diameter in the crystal were observed for the collinear geometry.

At high conversion efficiencies the beam divergence of the Raman laser was measured to be less than 40 mrad which would be consistent with a TEM_{00} mode divergence from a 250- μm -diameter laser cavity. The pump laser was operating in several higher-order modes which could account for the larger focal diameter. By converting the multitransverse mode pump beam to a single mode Raman beam, we have increased the brightness of the source.

Figure I-9 shows the output frequency of a spin-flip Raman laser as a function of magnetic field. In order to interpret the observed tuning characteristics, mode pulling must be

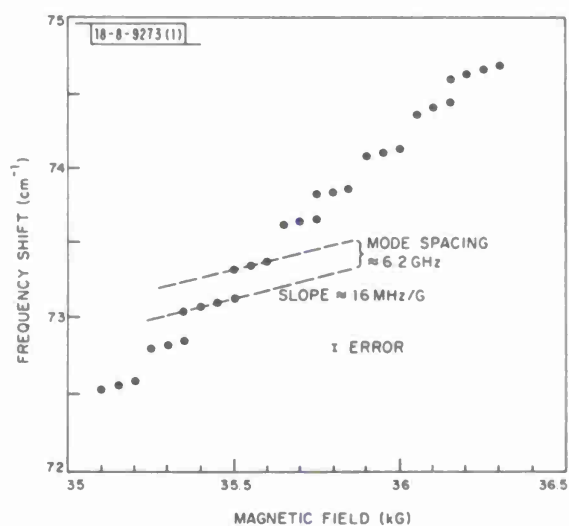


Fig. I-9. Variation of collinear geometry spin-flip Raman laser output frequency with magnetic field ($\lambda_{\text{pump}} = 5.32 \mu\text{m}$, $T \sim 30^\circ\text{K}$, concentration $\sim 1 \times 10^{16} \text{ cm}^{-3}$, sample length = 4.8 mm).

Section I

taken into account because the spontaneous Raman linewidth, Γ_s , is comparable to the cavity linewidth, Γ_c . In the case of a Lorentzian spontaneous line, the mode pulling is described by the equation³⁰

$$\nu = \frac{\nu_c \Gamma_s + \nu_s \Gamma_c}{\Gamma_s + \Gamma_c}, \quad (7)$$

where ν is the actual frequency of oscillation, and ν_c and ν_s are the peaks of the cavity and spontaneous scattering resonances, respectively. From Eq. (7) we obtain the spacing between two adjacent laser modes, $\Delta\nu$, at constant magnetic field,

$$\Delta\nu = \frac{30 \Gamma_s / (\Gamma_s + \Gamma_c)}{2l \left[n(\nu, H) + \nu \frac{\partial n(\nu, H)}{\partial \nu} \frac{\Gamma_s}{\Gamma_s + \Gamma_c} \right]} \text{ GHz}, \quad (8)$$

where l is the cavity length and $n(\nu, H)$ is the frequency and magnetic field dependent refractive index. By using the estimated parameters $\Gamma_s = 0.5 \text{ cm}^{-1}$ (obtained from preliminary lineshape fitting), $\Gamma_c = 0.15 \text{ cm}^{-1}$, $n = 3.9$ and the measured $\Delta\nu = 6.2 \text{ GHz}$, we obtain $\nu(\partial n/\partial \nu) = 0.4$. In laser diodes, $\Gamma_s \gg \Gamma_c$ so that the relevant parameter obtained from the mode spacing expression [Eq. (8)] is $n(\nu, H) + \nu \partial n(\nu, H)/\partial \nu$. Melngailis³¹ found a value of 5.2 for this quantity at a frequency much closer to the bandgap resonance, while we find a value of 4.3.

The frequency variation of a single mode with magnetic field is also obtained from Eq. (7) and is given by

$$\frac{d\nu}{dH} = \frac{\Gamma_c \frac{d\nu_s}{dH} - \frac{\nu \Gamma_s}{n} \frac{\partial n(\nu, H)}{\partial H}}{\Gamma_c + \Gamma_s \left[1 + \frac{\nu}{n} \frac{\partial n(\nu, H)}{\partial \nu} \right]}, \quad (9)$$

where the variation of Γ_c with ν and H has been neglected. If we use the measured value of $d\nu/dH = 16 \text{ MHz/G}$, we find that $\partial n/\partial H \approx -1 \times 10^{-7}/\text{G}$, which is about an order of magnitude lower than the measured values in PbTe and PbSe.³² It is important to note that variation of the refractive index with H alone (i.e., neglecting mode pulling) is the wrong sign to account for the observed frequency variation. The above values for the derivatives of the refractive index are only accurate to within a factor of two or three because of the approximations used; however, the calculations demonstrate that the mode hopping and pulling involved in the tuning of the spin-flip Raman laser can be explained by standard laser mode theory.

The line shape of the spontaneous spin-flip scattering was measured at 35 kG in a $1 \times 10^{16} \text{ cm}^{-3}$ and a $3 \times 10^{16} \text{ cm}^{-3}$ sample. The scattered light was collected along the magnetic field direction at right angles to the direction of the pump laser beam. The linewidth of the spontaneous scattering in the $1 \times 10^{16} \text{ cm}^{-3}$ sample was 1.5 cm^{-1} while for the $3 \times 10^{16} \text{ cm}^{-3}$ the linewidth was 3.3 cm^{-1} . The Raman frequency shift of the scattering from the $3 \times 10^{16} \text{ cm}^{-3}$ sample was 3.6 cm^{-1} less than that from the $1 \times 10^{16} \text{ cm}^{-3}$ sample. This difference can be accounted for by the nonparabolicity of the conduction band in InSb and the partial filling of the upper spin level in the higher concentration sample. The linewidth of the scattering from the

higher concentration sample is predominantly due to nonparabolicity, while that of the scattering from the lower density sample is attributable to both nonparabolicity and collisional broadening effects. There is an appreciable component of the linewidth which is due to collisional broadening in this case, since the dominant contribution to the spin-flip scattering arises from electrons near the bottom of the conduction band where the nonparabolicity broadening is minimal.

This high power single mode operation greatly enhances the potential of this device for use in high resolution infrared spectroscopy and heterodyning applications.

S. R. J. Brueck
A. Mooradian

REFERENCES

1. Solid State Research Report, Lincoln Laboratory, M.I.T. (1970:3), p. 8, DDC AD-714079.
2. I. Melngailis and A. R. Calawa, Appl. Physics Letters 9, 304 (1966), DDC AD-648772; Solid State Research Report, Lincoln Laboratory, M.I.T. (1966:4), p. 1, DDC AD-647688.
3. J. F. Butler and T. C. Harman, Appl. Phys. Letters 12, 347 (1968), DDC AD-673601.
4. A. J. Strauss, private communication.
5. M. A. Gilleo, P. T. Bailey and D. E. Hill, Phys. Rev. 174, 898 (1968).
6. E. H. Bogardus and H. B. Bebb, Phys. Rev. 176, 993 (1968).
7. J. Shah, R. C. C. Leite and J. P. Gordon, Phys. Rev. 176, 938 (1968).
8. R. Dingle and K. F. Rodgers, Jr., Appl. Phys. Letters 14, 183 (1969).
9. R. Dingle, Phys. Rev. 184, 788 (1969).
10. E. W. Williams and H. Bebb, J. Phys. Chem. Solids 30, 1289 (1968).
11. D. E. Hill, Phys. Rev. B 1, 1863 (1970).
12. W. Schairer and W. Graman, J. Phys. Chem. Solids 30, 2225 (1969).
13. C. M. Wolfe, G. E. Stillman and J. O. Dimmock, J. Appl. Phys. 41, 504 (1970).
14. J. A. Rossi, G. E. Stillman, C. M. Wolfe and J. O. Dimmock, Solid State Commun. 15, 2021 (1971).
15. G. E. Stillman, C. M. Wolfe and J. O. Dimmock, Solid State Commun. 7, 921 (1969).
16. G. E. Stillman, C. M. Wolfe and J. O. Dimmock, J. Phys. Chem. Solids 31, 1199 (1970).
17. D. G. Thomas, M. Gershenson, and F. A. Trumbore, Phys. Rev. 133, 269 (1964).
18. D. M. Larsen, J. Phys. Chem. Solids 29, 271 (1968).
19. See A. C. Beer, Galvanomagnetic Effects in Semiconductors (Academic Press, New York, 1963), p. 308; R. T. Bate, in Semiconductors and Semimetals, Vol. 4, Physics of III-V Compounds, R. K. Willardson and A. C. Beer, Eds. (Academic Press, New York, 1968), p. 459.
20. See L. R. Weisberg, J. Appl. Phys. 33, 1817 (1962).
21. D. Colman and D. L. Kendall, J. Appl. Phys. 40, 4662 (1969).
22. F. V. Williams and D. Hill, private communication.
23. G. A. Antcliffe and J. S. Wrobel, Mat. Res. Bull. 5, 747 (1970).

Section I

24. L. J. van der Pauw, Philips Res. Rept. 13, 1 (1958).
25. C. Herring, J. Appl. Phys. 31, 1939 (1960).
26. A. Mooradian, S. R. J. Brueck, and F. A. Blum, Appl. Phys. Letters 17, 481 (1970).
27. Y. Yafet, Phys. Rev. 152, 858 (1966).
28. G. B. Wright, P. L. Kelley, and S. H. Groves, in Light Scattering Spectra of Solids, G. B. Wright, Ed. (Springer-Verlag, New York, 1969), p. 335.
29. C. K. N. Patel and E. D. Shaw, Phys. Rev. Letters 24, 451 (1970); C. K. N. Patel in Proceedings Tenth International Conference on the Physics of Semiconductors, S. P. Keller, J. C. Hensel, and F. Stern, Eds. (AEC, Oak Ridge, 1970), p. 746.
30. W. R. Bennett, Jr., Appl. Opt., Suppl. I: Optical Masers, 24 (1962); see also, G. Birnbaum, Optical Masers (Academic Press, New York 1964).
31. I. Melngailis, Appl. Phys. Letters 6, 59 (1965).
32. J. F. Butler and A. R. Calawa, in Physics of Quantum Electronics, P. L. Kelley, B. Lax and P. E. Tannenwald, Eds. (McGraw Hill, New York, 1966), p. 458.

II. MATERIALS RESEARCH

A. SEALED CRUCIBLE TECHNIQUE FOR THERMAL ANALYSIS OF VOLATILE COMPOUNDS UP TO 2500°C

Thermal analysis is particularly difficult for compounds that have vapor pressures above a few torrs or melting points above 2000°C. We have developed a thermal analysis system which utilizes welded crucibles of refractory metals to contain the samples and tungsten-tungsten (rhenium) thermocouples to record thermal arrests at temperatures up to about 2500°C.

Many of the more refractory metals are potentially suitable for crucible use at high temperatures because they have a low affinity for oxygen and other nonmetallic elements. A number of such metals are listed in Table II-1 along with their melting points and pO values, where pO is the negative log of the oxygen pressure at 1000°K characteristic of the equilibrium between the metal and its lowest oxide.¹ Some compounds that we have melted in these crucibles are also listed in Table II-1. In general we have found that if no obvious reaction occurs between the compound and the crucible, the contamination of the melt by the crucible metal is below the 10 ppm level. This is probably due to the fact that the oxides of all the metals listed except tantalum are volatile above 1800°K.

Two types of crucibles used for thermal analysis are shown in Fig. II-1. We have used molybdenum for these crucibles, which have a thermocouple well in the lid, because it can be machined relatively easily. After being loaded with the sample material, the crucibles are welded in a simple arc furnace described previously.²

The furnace for thermal analysis is shown schematically in Fig. II-2. It consists of a water-cooled stainless steel shell containing a tungsten or tantalum resistance-heated element surrounded

TABLE II-1
METALS FOR HIGH-TEMPERATURE CRUCIBLES

Metal	Melting Point (°C)	pO	Melts Contained
Platinum	1769	-1.3	
Iridium	2454	0.9	Al ₂ O ₃ , CaWO ₄ , SnO ₂
Rhenium	3180	13.6	ZnS, ZnSe
Molybdenum	2610	20.1	Al ₂ O ₃ , EuO, EuSe, EuTe, YAG, Y ₂ O ₂ S, CdSe, Ti ₂ O ₃ , GdTiO ₃
Tungsten	3410	21.2	Al ₂ O ₃ , EuO, EuSe, EuTe, EuS, YAG

Section II

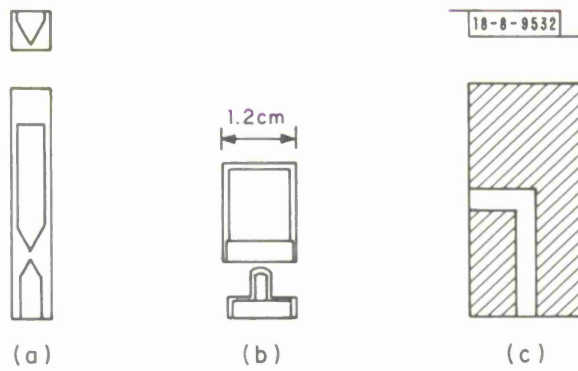


Fig. II-1. (a) and (b) Molybdenum crucibles with thermocouple well for thermal analysis. (c) Sighting block for pyrometer calibration.

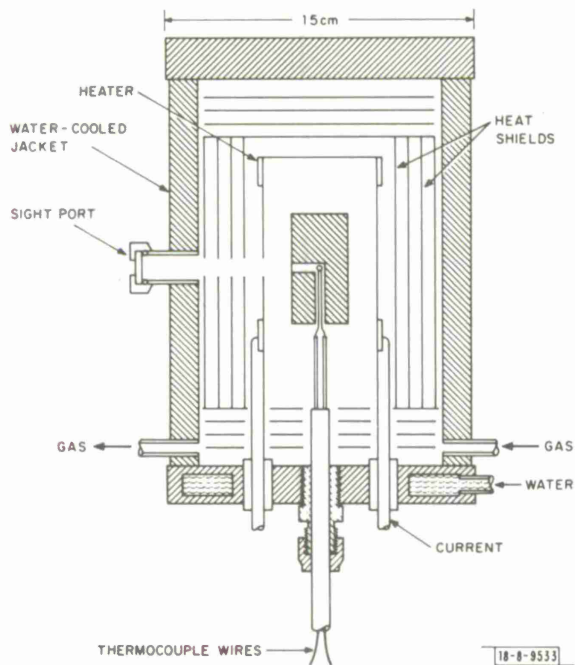


Fig. II-2. Schematic view of furnace for thermal analysis to 2500°C, showing W-W (0.26 Re) thermocouple in sighting block for calibrating thermocouple against pyrometer.

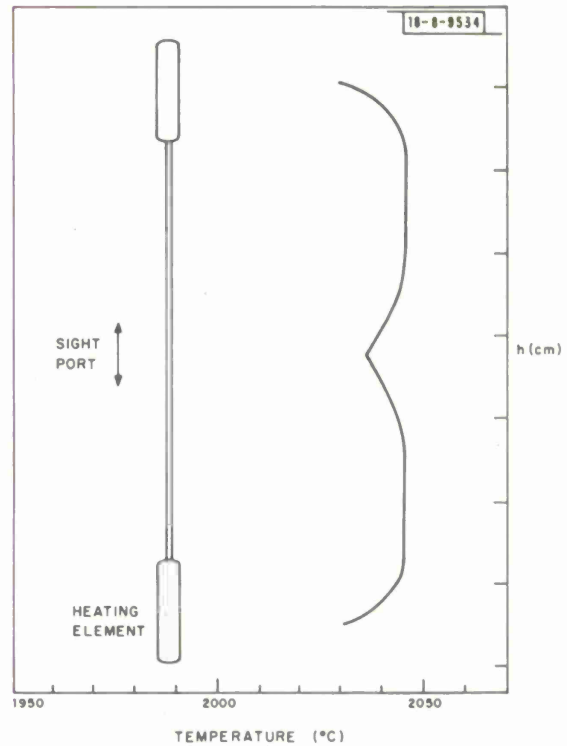


Fig. II-3. Typical temperature profile of hot zone of furnace as measured by sliding thermocouple.

by tantalum heat shields which lower the power requirement and help to establish blackbody conditions in the hot zone of the furnace. A typical temperature profile of the hot zone, measured with a movable thermocouple, is shown in Fig. II-3. The maximum operating temperature of the furnace with a tungsten element and tantalum shields is about 2600°C. The temperature can be programmed to increase or decrease at 5° to 5000°C/hour. Thermal analysis is generally performed under a slight positive pressure of argon maintained by slowly passing titanium-gettered argon through the furnace and then through a bubbler. However, runs can be made in vacuum to remove volatile impurities from compounds in open crucibles, to remove contamination from the heat shields or to eliminate arcing at very high temperatures.

Tungsten-tungsten (0.26 Re) and tungsten (0.05 Re) - tungsten (0.26 Re) thermocouples are made from 0.75-mm wire and welded in the arc furnace used for welding crucibles. It is necessary to give the thermocouple its final shape before welding, since afterward the wire is extremely brittle. A number of ceramics have been tested for thermocouple insulation above 2000°C, the upper limit of usefulness for alumina tubing. Both MgO and BeO warped and evaporated badly above 2000°C, contaminating the furnace. Although ZrO₂ and ThO₂ have high melting points, they become good conductors at higher temperatures. When thermocouple wires were mounted in two-hole thermocouple tubing of ZrO₂ or ThO₂ without making a junction, the resistance between the wires (i.e., across the ceramic) was about 9 ohms at 2000°C. Since the resistance in the thermocouple wire is less than 0.01 ohm, this resistance short circuit does not alter the thermocouple reading. Nevertheless, to eliminate conduction through the ceramic, the thermocouple wires for the thermal analysis measurements were mounted in two separate thoria tubes, as shown in Fig. II-2. To observe the thermal arrests the thermocouple voltage (filtered by a capacitor network to reduce noise and balanced with a microvolt potentiometer to increase sensitivity) was monitored with a recording potentiometer.

The thermocouple calibration was checked by placing a thermocouple in a sighting block [shown in Fig. II-1(c)], heating the block in the furnace, and measuring the temperature of the block with an optical pyrometer which we had calibrated against an NBS tungsten ribbon standard lamp. When a correction of +5°C was made for the sighting window in the furnace, the measurements in the range 1500° to 2500°C agreed within 5°C with the calibration curves supplied by the thermocouple manufacturer. Similar agreement was obtained between optical pyrometer and thermocouple measurements of crucible temperatures during thermal analysis.

Single crystals were used as the starting material in most of the melting point determinations. The measurements were made by observing the thermal arrests which occurred when the sample was slowly heated or cooled in the vicinity of the melting point. In some cases the furnace was returned to the arrest temperature and a measurement was made with the optical pyrometer as a guard against faulty thermocouple readings. Illustrative recorder traces, obtained in measurements on sapphire, are shown in Fig. II-4. Good agreement was generally found between the melting and freezing arrests (curves A and B). However, if sapphire samples were heated more than 50°C above the melting point (curve C), supercooling as much as 170°C occurred (curve D), and the temperature during freezing never reached the melting point. To avoid such supercooling difficulties, samples of all compounds were usually heated not more than 20°C above their melting points before cooling. Varying the cooling rate between 5° and 350°C/min did not significantly affect the measured melting points, except at the highest rate.

Section II

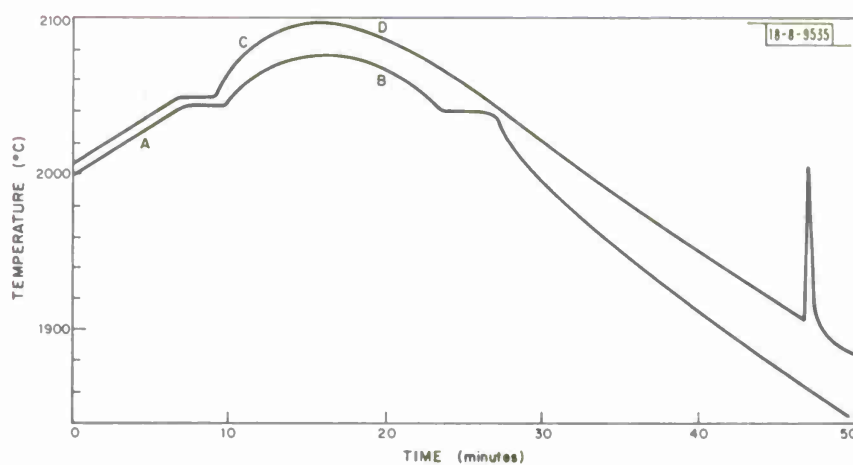


Fig. II-4. Recorder traces obtained in thermal analysis experiments on sapphire. A. Heating curve. B. Cooling curve. C. Heating curve to 60°C above melting point. D. Cooling curve after heating to 60°C above melting point.

Compound	Melting Point (°C)	Range (°C)	Number of Thermal Arrests	Maximum Supercooling (°C)	Melting Point (°C)
Al ₂ O ₃	2044	±5	30	170	2045*
EuO	1976	±8	85	10	
EuS	2490	±40	1	None	
EuSe	2210	±8	9	70	
EuTe	2183	±2	21	70	
YAG	1967	±5	2		
ZnSe	1513		1		1515†
CdSe	1235		12	4	1239-1264

* Ref. 3.
† Ref. 6.

Melting point measurements have been made on sapphire and YAG (yttrium aluminum garnet), on the four europium monochalcogenides and on ZnSe and CdSe, two volatile compounds with lower melting points. The results are listed in Table II-2, together with literature values if available. The melting point obtained for sapphire agrees with the latest accepted value.³ Some supercooling was observed for all the europium chalcogenides and superheating occurred several times on melting EuO. The melting points measured for the europium compounds are consistent with observations made during many crystal growth experiments.⁴ EuS has the highest melting point, 2490°C, and several times unmelted crystals were found after unsuccessful growth runs in crucibles that had been taken to ~2450°C before cooling.

An attempt was made to measure the melting point of YAG.⁵ On first heating and cooling, arrests were observed at 1968°C, but on heating to a higher temperature and cooling no arrest was seen at this temperature and several other arrests appeared. This suggests that either some decomposition occurred or that the melting is not congruent.

T. B. Reed
R. E. Fahey
A. J. Strauss

B. EFFECT OF PRESSURE ON MAGNETIC PROPERTIES OF $\text{Ca}_{1-x}\text{Sr}_x\text{MnO}_3$

Oxides with the formula ABO_3 and perovskite structure would appear to be good systems for studying the effect of lattice dimension on magnetic interactions. The only important magnetic interaction is an ~180° B-O-B interaction along the pseudocubic edge, and competing next-neighbor interactions are small. In addition, a large number of chemical substitutions are permissible within this structure.

MacChesney, *et al.*,⁷ studied the effect of substituting Sr for Ca in $\text{Ca}_{1-x}\text{Sr}_x\text{MnO}_3$, in which Mn^{4+} ions are at the B-cation sites. An increase in the Sr content increases the cell dimensions and Néel temperature (T_N) while decreasing the distortion and magnetic moment (σ). If the effect of the chemical substitution is purely dimensional, $dT_N/da_0 > 0$ is a surprising result for localized d-electrons. However, Goodenough⁸ pointed out that covalent mixing of A-site cations with the anion p_π orbitals competes with covalent mixing of the B-cation d-orbitals of t_{2g} symmetry, thereby reducing the B-O-B interaction, and concluded that the increase in T_N with increased Sr content was due to Sr being less covalent than Ca. Also, since comparison with other perovskite systems indicates that the Mn^{4+} 3d electrons occupy localized t_{2g} orbitals,⁹ Goodenough⁸ predicted $dT_N/da_0 < 0$ in CaMnO_3 . This was confirmed by the experimental observation that $dT_N/dP > 0$. An alternative explanation is that the change in T_N with pressure is primarily due to a change in the departure of the B-O-B interaction angle from 180°. Treves, Eibschütz, and Coppens¹⁰ have shown such an effect in the orthoferrites.

In this investigation we have measured the effect of pressure on T_N and σ in the system $\text{Ca}_{1-x}\text{Sr}_x\text{MnO}_3$ for compositions of $x = 0, 0.15, 0.25,$ and 0.50 . The investigation was initiated (1) to see whether our result¹¹ for CaMnO_3 extended throughout the system, (2) to attempt to distinguish between the relative importance for T_N of covalency⁸ and interaction-angle effects,¹⁰ and (3) to determine the effect of pressure on the weak ferromagnetism of the members of the system.

The magnetic measurements were performed on a vibrating-coil magnetometer used in conjunction with a helium-gas unit for generating hydrostatic pressure.¹¹ To prepare the

Section II

samples, stoichiometric mixtures of SrCo_3 , CaCO_3 and MnO were fired in air at 1400°C in alundum boats for periods up to a week with daily regrindings. The resulting material was oxygen deficient, but after being annealed in oxygen at 400°C for 16 hours, it was shown to be single phase by powder x-ray diffraction techniques and was found to contain 3.00 ± 0.05 oxygen atoms per formula by TGA analysis in H_2 -Ar. The unit-cell dimensions of our samples are in good agreement with those reported by MacChesney, *et al.*,⁷ which are limited to $x \leq 0.25$. The cell volume continues to expand smoothly up to $x = 0.50$.

All the samples are basically antiferromagnetic but exhibit weak ferromagnetism below T_N . To study the spontaneous moment, all measurements were carried out on a magnetic field of 100 Oe, where induced effects are negligible. To ensure that the spontaneous moment aligned itself along the easy direction nearest the field, measurements were made only after cooling the sample through T_N in the presence of an applied field. The Néel points were obtained by extrapolating the maximum slope of the σ versus T curve to zero moment. The atmospheric pressure T_N values are in good agreement with those found previously.⁷ The values of dT_N/dP are all positive and exhibit only a small variation with x (see Table II-3). The slightly larger error bracket for dT_N/dP at $x = 0.25$ is due to a significant change in shape of the magnetization versus temperature curve as a function of pressure, while the large uncertainty at $x = 0.5$ is due to the low spontaneous moment in that sample. The variation of σ with T at atmospheric pressure is shown in Fig. II-5. The values of σ for $x = 0$ and $x = 0.15$ are in reasonable accord with those obtained by MacChesney, *et al.*,⁷ on the basis of measurements at 14 kOe; however, our value for $x = 0.25$ is significantly lower than theirs, at least partially due to the difference in measurement techniques.

x	T_N ($^\circ\text{K}$)	dT_N/dP ($^\circ\text{K}/\text{kbar}$)
0	125	$+0.42 \pm 0.02$
0.15	139	$+0.44 \pm 0.02$
0.25	147.5	$+0.38 \pm 0.03$
0.50	174.5	$+0.55 \pm 0.25$

The effect of pressure on the weak ferromagnetic moment was also studied at fixed temperatures $T < T_N$ in a field of 100 Oe. The results, given in Fig. II-6 for $x = 0$, 0.15 and 0.25, indicate a reduction in moment with increasing pressure. A dramatic increase in $|\sigma/dP|$ occurs at $x = 0.25$. A small decrease in σ with increasing pressure was observed at $x = 0.5$, but with considerable uncertainty owing to the smallness of the net moment.

In perovskite-like structures, it is only the distortion from the ideal cubic structure that permits the existence of weak ferromagnetism. Furthermore, the small relative change of T_N with pressure observed in our samples indicates that both the exchange interaction and the total spin of the magnetic ions are only weakly affected by pressure. Under these conditions it is

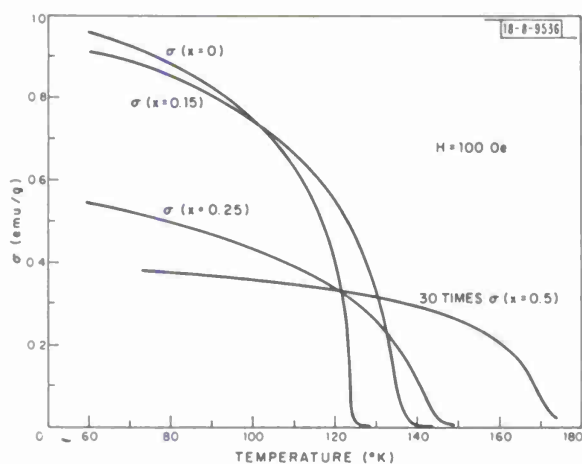


Fig. II-5. Magnetic moment versus temperature in $\text{Ca}_{1-x}\text{Sr}_x\text{MnO}_3$ at atmospheric pressure.

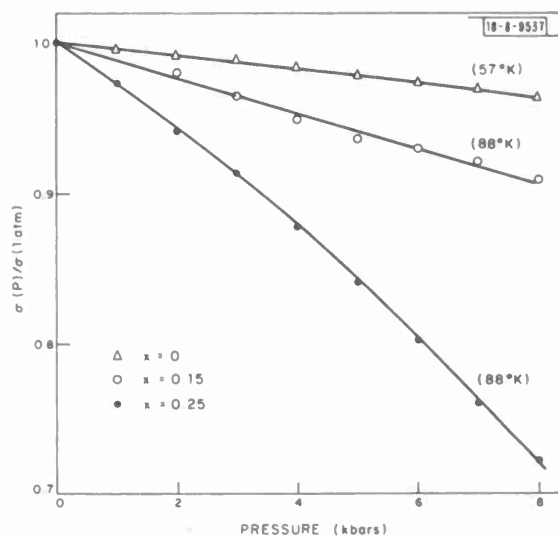


Fig. II-6. Variation of magnetic moment with pressure in $\text{Ca}_{1-x}\text{Sr}_x\text{MnO}_3$ at fixed temperature.

implicit in the Moriya¹² formalism that the significant reduction in moment with pressure is correlated with a reduction in the orthorhombic distortion and hence reflects a reduction in the deviation of the B-O-B exchange interaction angle from 180°.

The observed increase in T_N with pressure is in accord with the premise of Treves, *et al.*,¹⁰ that such an increase can be attributed to an increase in the B-O-B angle toward 180°. However, were this the major factor, the marked increase in $|d\sigma/dP|$ at $x = 0.25$ would lead one to expect a similar increase in dT_N/dP at this composition. This is not observed. The approximate equality of dT_N/dP at all values of x appears more consistent with the model proposed by Goodenough.⁸ The present results strikingly point up the danger inherent in the assumption that the effect on magnetic properties of substituting one "magnetically neutral" ion for another is equivalent to a simple change in the lattice dimensions. Chemical effects are clearly of critical importance and can, in fact, completely overwhelm size effects.

J. A. Kafalas J. M. Longo
N. Menyuk D. A. Batson
K. Dwight D. M. Tracy

C. TWO DISTINGUISHABLE MECHANISMS IN SEMICONDUCTOR-TO-METAL TRANSITION IN VO_2

From symmetry arguments, a nearly isotropic resistivity, an anisotropic thermal expansion, and optical data, it is possible to construct the one-electron energy model of high-temperature, tetragonal VO_2 shown in Fig. II-7. The Fermi energy intersects two bands: a pseudodegenerate π^* band and a $d_{||}$ band. The total number of occupied states in these two bands is one per formula unit, corresponding to a vanadium-ion formal valence V^{4+} . Itinerant-electron π^* orbitals follow from two observations: (1) In the tetragonal (rutile) structure, each anion σ bonds with three, coplanar nearest-neighbor cations and has one p_π orbital perpendicular to this plane available for π bonding with two cation d orbitals, labeled d_π . (2) The perovskites

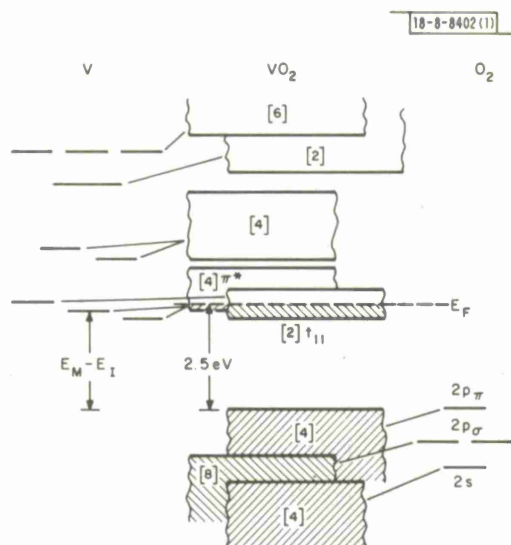


Fig. II-7. One-electron band structure for tetragonal VO_2 .

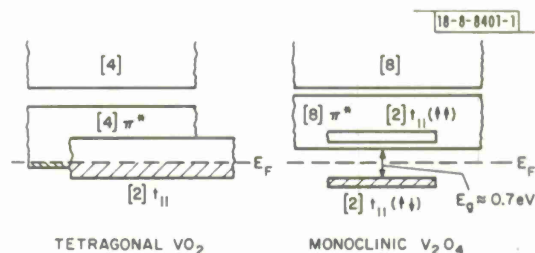


Fig. II-8. Schematic modification of d-band structure of VO_2 on passing from metallic to semiconducting phase.

CaVO_3 and SrVO_3 are metallic and Pauli paramagnetic, showing that $\text{V}^{4+}-\text{O}^{2-}:p_{\pi}-\text{V}^{4+}$ interactions are strong enough to delocalize d_{π} electrons. In the rutile structure, occupied anion octahedra form edge-shared chains parallel to the c_r axis, and the V-V separation $R = 2.88 \text{ \AA}$ is smaller than the critical distance $R_c(\text{V}^{4+}) = 2.94 \text{ \AA}$. Therefore, these form a cation-sublattice $d_{||}$ band. However, with only two like near neighbors, R is close enough to R_c that the $d_{||}$ band must be narrow; and a temperature-dependent magnetic susceptibility, which signals the presence of exchange enhancement, testifies to the importance of electron correlations in this band.

Below $T_t = 340^\circ\text{K}$, VO_2 is a semiconductor, a discontinuity in resistivity of over four orders of magnitude occurring in pure, stoichiometric samples. This fact requires that at low temperatures the energy-band model of Fig. II-7 must be modified as follows: The π^* bands must be raised above E_F , and the resulting half-filled $d_{||}$ band must be split in two as shown in Fig. II-8. There are three ways to accomplish this modification: (1) Raise the π^* bands relative to the $d_{||}$ band by an antiferroelectric distortion that widens the gap between π and π^* bands while simultaneously splitting the $d_{||}$ band in two. (2) Lower the occupied $d_{||}$ energies relative to the π^* bands by (a) decreasing the crystallographic ratio c_r/a_r and/or (b) splitting the $d_{||}$ band in two either by antiferromagnetic ordering along the c_r axis or by forming V-V pairs along c_r such that $R < R_c$ within homopolar-bonded pairs and $R > R_c$ between pairs. NMR and Mossbauer measurements rule out any antiferromagnetic ordering. Consideration of a variety of doping experiments has led to the following model, which is now being checked directly by a structure refinement of Cr-doped VO_2 .

Two components of the low-temperature, monoclinic structure of VO_2 can be distinguished: an antiferroelectric component and a V-V pairing along the $a_m = 2c_r$ axis as a result of homopolar bonding via the single d electron per V^{4+} ion.

In several $V_{1-x}M_xO_2$ systems, namely, $M = Cr, Fe, Ga, Al, Ti$ and Ge , even initial additions of M ($x < 0.001$) separate the two components of the distortion, so that the monoclinic phase appears only at $T < T_t$, an orthorhombic phase having $c_o = 2c_r$ and $a_o \approx b_o \approx 2\sqrt{2a_t}$ occurring in the interval $T'_t < T < T_t$. Since an antiferroelectric distortion is, in itself, capable of producing a semiconductor-to-metal transition, the orthorhombic phase is presumed to be antiferroelectric. It is this presumption that is being checked by a structure refinement. For small x , a semiconductor-to-metal transition occurs across T_t , a semiconductor-to-semiconductor transition across T'_t . The formation of V-V pairs along $a_m = 2c_r$ in the monoclinic phase increases the splitting of the $d_{||}$ band, and hence the energy gap below T'_t .

Since splitting of the $d_{||}$ band is energetically favorable only if the band is half-filled (or nearly half-filled), homopolar-band formation is contingent on the antiferroelectric component of the distortion, which raises the π^* bands above E_F . Therefore, the constraint $T'_t \leq T_t$ must hold, and the driving force for the transition is the antiferroelectric component of the distortion. The equality $T'_t = T_t$ in pure VO_2 is a coincidence, and even hydrostatic pressure may separate the two temperatures.

Substitution of foreign cations, which cannot participate in cooperative V-V homopolar bonding, necessarily decreases T'_t . The condition for the appearance of an orthorhombic phase in the interval $T'_t < T < T_t$ in the systems $V_{1-x}M_xO_2$ is

$$dT'_t/dx < dT_t/dx \quad , \quad (1)$$

and where $dT_t/dx > 0$, the orthorhombic phase always appears.

Addition of M^{3+} ions creates discrete V^{5+} ions trapped at the M^{3+} -ion centers, and V^{5+} ions are not stable in sixfold coordination. Therefore, they stabilize an antiferroelectric distortion, and $dT_t/dx > 0$. Similarly, Ge^{4+} is unstable in a sixfold coordination, making $dT_t/dx > 0$. The Ti^{4+} ion, though stable in sixfold coordination, readily participates in a cooperative, antiferroelectric distortion (e.g., $BaTiO_3$). Although $dT_t/dx < 0$ occurs in $V_{1-x}Ti_xO_2$, its magnitude is relatively small and the condition of Eq. (1) is satisfied. In systems $V_{1-x}M_xO_2$ having other M ions, this condition is not fulfilled. However, there the constraint $T'_t < T_t$ keeps $dT'_t/dx = eT_t/dx$, and there is only one transition: from monoclinic to tetragonal as in VO_2 .

Changes in the resistivity discontinuity $\Delta\rho$ across T_t for different solute atoms M can also be rationalized with this band model.

J. B. Goodenough

D. FREE-CARRIER ABSORPTION IN n-TYPE PbTe

The optical absorption coefficients of n-type PbTe samples with carrier concentrations between 9×10^{16} and $5 \times 10^{18} \text{ cm}^{-3}$ have been measured at room temperature for wavelengths between 6 and 15 μm , in order to determine whether free-carrier absorption is the dominant absorption mechanism in this wavelength region lying just beyond the intrinsic absorption edge. If free-carrier absorption is dominant even for the samples with the lowest carrier concentrations, material that is more transparent cannot be prepared unless the carrier concentration can be reduced still further.

The samples were single crystals cut from ingots grown from the melt either by the vertical Bridgman method or by horizontal zone melting. The as-grown material was p-type, with hole

Section II

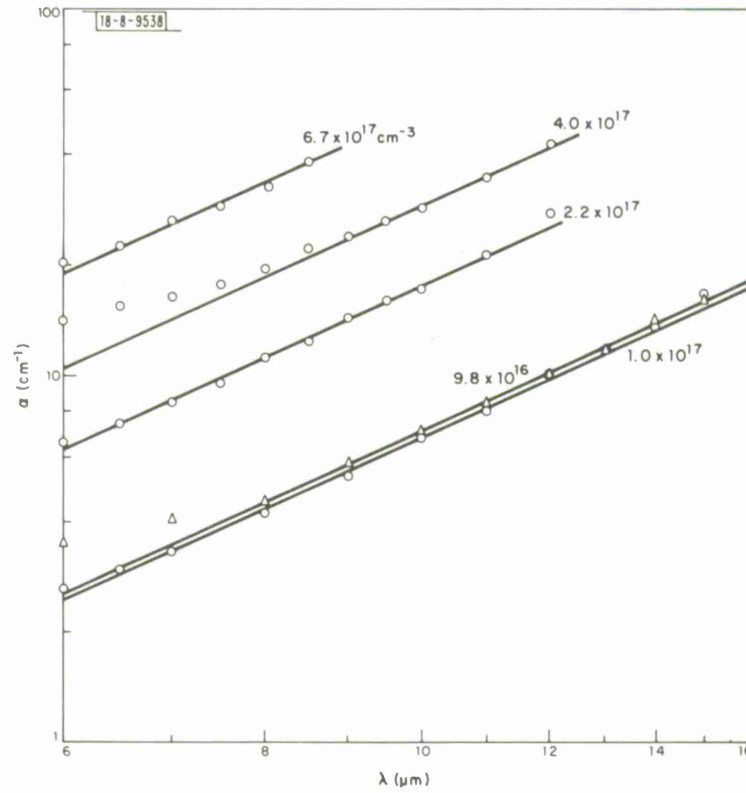


Fig. II-9. Dependence of absorption coefficient at room temperature on wavelength for n-type PbTe samples with carrier concentrations given.

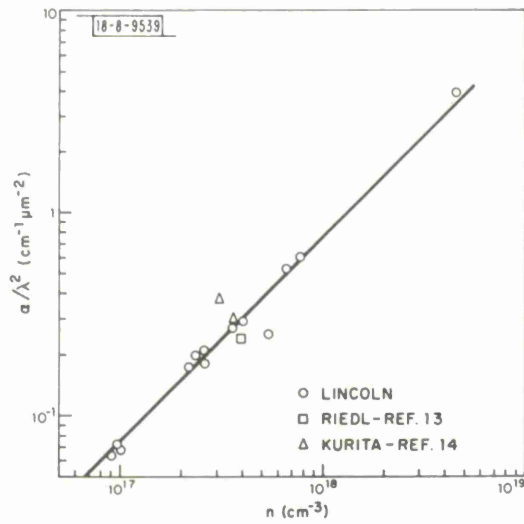


Fig. II-10. Dependence of α/λ^2 ratio on carrier concentration for n-type PbTe.

concentrations above 10^{18} cm^{-3} due to the presence of Te in excess of the stoichiometric composition. To convert the samples to n-type by replacing the excess Te with excess Pb, in most cases they were first annealed at 850° to 860°C for 16 hours in sealed quartz ampoules containing a two-phase mixture of Pb and Pb-saturated PbTe and then quenched into water. The carrier concentration was adjusted by subsequent annealing at lower temperatures, sometimes with a Pb-rich mixture and sometimes without, which changed the concentration of excess Pb either by equilibration with the vapor phase or by internal precipitation of Pb exceeding the solubility at the annealing temperature. The lowest carrier concentrations were obtained in samples which were annealed at 400°C for more than 2 weeks. The maximum concentration was obtained in a sample from a Bi-doped ingot; the other samples were from ingots that had not been intentionally doped.

The absorption coefficient (α) measured at room temperature for several representative samples of n-type PbTe is plotted against wavelength (λ) on a log-log scale in Fig. II-9. Most of the data are consistent with free-carrier absorption, since they are well represented by a series of parallel straight lines with slope of 2, corresponding to the λ^2 dependence given by the classical expression for this absorption mechanism. In some cases, however, the absorption coefficients at the shorter wavelengths lie above the straight line, indicating the presence of an additional absorption mechanism in this region.

For classical free-carrier absorption, the absorption coefficient at a fixed wavelength is proportional to the carrier concentration (n), provided that the effective mass and mobility are independent of n . For most of the samples measured, such a linear dependence is observed in the wavelength region where α is proportional to λ^2 . This is shown by Fig. II-10, in which values of α/λ^2 for the straight lines in Fig. II-9 and for similar lines obtained for the other samples measured are plotted on a log-log scale against values of n determined by Hall coefficient measurements at room temperature. Most of the points, including those for 3 samples reported in the literature,^{13,14} fall close to the straight line shown, which has a slope of 1. The value of $\alpha/n\lambda^2$ for this line is $7.5 \times 10^{-19} (\text{cm}/\mu\text{m})^2$. The effective mass, m^*/m_0 , calculated from this value according to the classical free-carrier expression (assuming a refractive index of 5.7 and mobility of $1.5 \times 10^3 \text{ cm}^2/\text{V-sec}$) is 0.091, in reasonable agreement with a value of 0.103 for the conductivity effective mass at 300°K obtained¹⁵ from infrared reflectivity measurements on samples with carrier concentrations of 2 to $4 \times 10^{18} \text{ cm}^{-3}$.

The data of Figs. II-9 and II-10 indicate that free-carrier absorption is the dominant absorption mechanism at room temperature over the wavelength range studied for our samples of n-type PbTe with carrier concentrations of 9×10^{16} – $1 \times 10^{17} \text{ cm}^{-3}$, the lowest values we have obtained. Therefore, it will be necessary to prepare samples with still lower carrier concentrations in order to reduce the optical absorption at room temperature.

A. J. Strauss

Section II

REFERENCES

1. T. B. Reed and E. R. Pollard, *J. Crystal Growth* 2, 243 (1968), DDC AD-681576.
2. T. B. Reed, "Arc Techniques for Material Preparation and Czochralski Crystal Growth," in High Temperature Technology (Butterworths, London, 1967).
3. S. J. Schneider and C. L. McDaniel, *J. Res. Natl. Bur. Std. A. Physics and Chemistry* 71A (1967).
4. T. B. Reed and R. E. Fahey, *J. Crystal Growth* 8, 337 (1971).
5. Supplied by R. Putbach, Airtron Corp., a Division of Litton Industries.
6. A. Libicky, *International Conference II-VI Semiconducting Compounds* (1967).
7. J. B. MacChesney, H. J. Williams, J. F. Potter and R. C. Sherwood, *Phys. Rev.* 164, 779 (1967).
8. J. B. Goodenough, *Phys. Rev.* 164, 785 (1967).
9. J. B. Goodenough and J. M. Longo, Landolt-Bornstein, Vol. III/4a (Springer-Verlag, Berlin, 1970).
10. D. Treves, M. Eibschütz and P. Coppens, *Phys. Letters* 18, 216 (1965).
11. N. Menyuk, J. A. Kafalas, K. Dwight and J. B. Goodenough, *J. Appl. Phys.* 40, 1324 (1969).
12. T. Moriya, *Phys. Rev.* 120, 91 (1960).
13. H. R. Riedl, *Phys. Rev.* 127, 162 (1962).
14. S. Kurita, I. Nagasawa, K. Tanaka, Y. Nishina and T. Fukuroi, *Sci. Repts. Res. Inst. Tohoku Univ.* 17, 37 (1965).
15. H. A. Lyden, *Phys. Rev.* 135, A514 (1964).

III. PHYSICS OF SOLIDS

A. ELECTRONIC BAND STRUCTURE

1. Galvanomagnetic Measurements at Hydrostatic Pressure on $\text{Hg}_{1-x}\text{Cd}_x\text{Te}$ Alloys, near Semimetal-Semiconductor Transition

Measurements of Hall coefficient, resistivity and their magnetic field dependence have been made on p-type samples of $\text{Hg}_{1-x}\text{Cd}_x\text{Te}$ in which the energy gap was varied from a negative or very small positive value up to approximately 0.06 eV by the application of hydrostatic pressure. Results have been obtained at 77°, 4.2° and 1.3°K. In the semimetallic region the minority electrons make a significant contribution to the transport properties because of the high electron-to-hole mobility ratio. Therefore, in the contrast to earlier measurements on n-type samples,¹ large changes in the resistivity and the low field Hall coefficient occur when the energy gap is opened with pressure. This is illustrated by the results shown in Fig. III-1. A clear indication

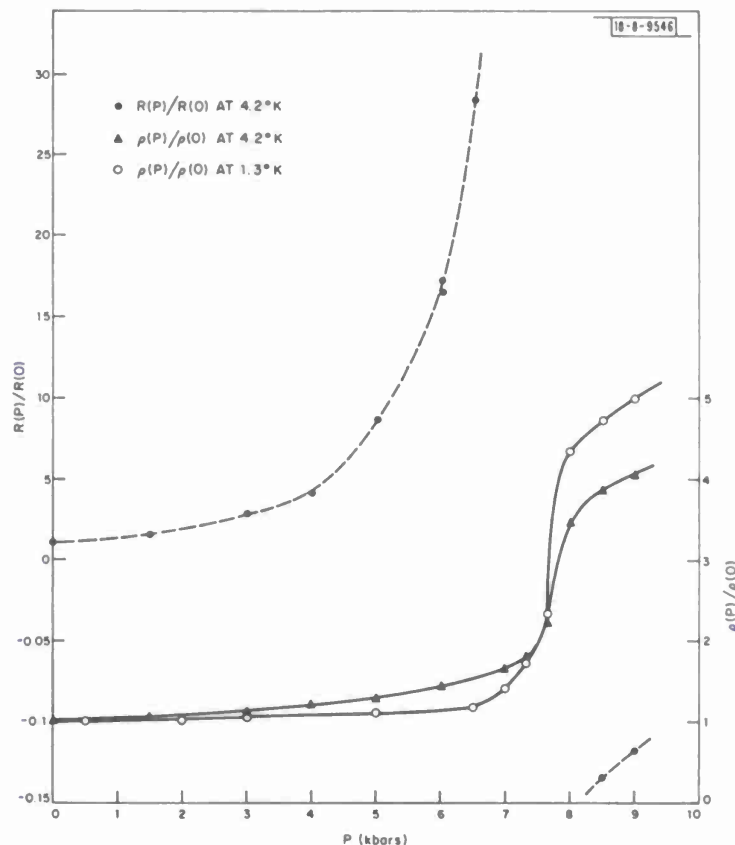


Fig. III-1. Relative variation of zero field Hall coefficient and resistivity of $\text{Hg}_{0.86}\text{Cd}_{0.14}\text{Te}$ as a function of pressure. Scale for $R(P)/R(0)$, which is on the left, changes for negative values. Hall coefficient rises sharply to 8 kbars and changes sign between 8 and 8.5 kbars. Relative resistivity $\rho(P)/\rho(0)$ increases sharply between 7 and 8 kbars.

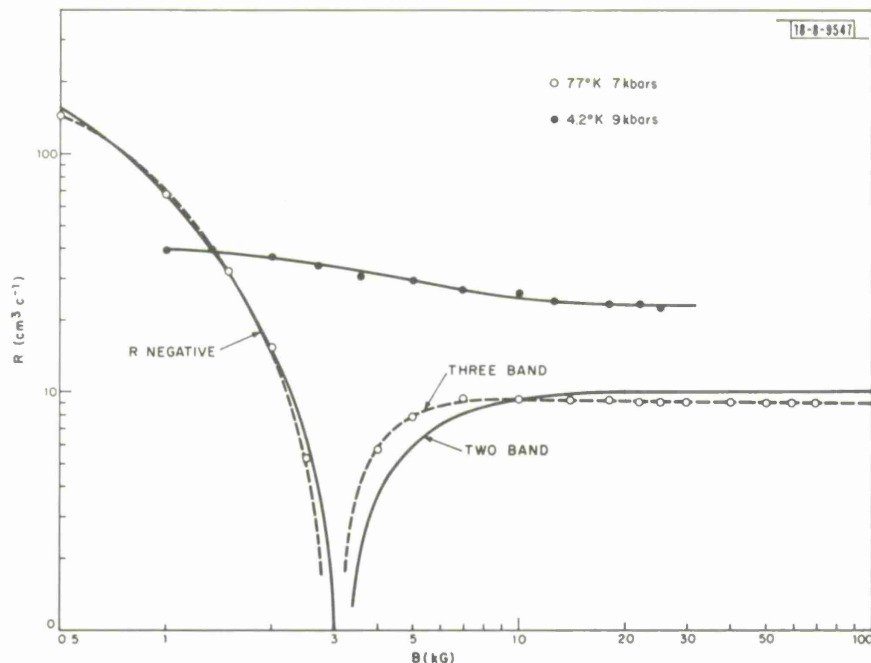


Fig. III-2. Hall coefficient as a function of magnetic field for sample with $x = 0.14$. Two sets of experimental data are shown, one obtained at 77°K and 7 kbars; the other, at 4.2°K and 9 kbars. Lines give results of least-squares fitting. For 4.2°K data, carrier concentrations were $2.7 \times 10^{17} \text{ cm}^{-3}$ heavy holes and $3.6 \times 10^{13} \text{ cm}^{-3}$ light holes. At 77°K , carrier concentrations were $7.0 \times 10^{17} \text{ cm}^{-3}$ heavy holes, $4.8 \times 10^{13} \text{ cm}^{-3}$ light holes and $3.0 \times 10^{13} \text{ cm}^{-3}$ electrons for three-band fit; and $6.0 \times 10^{17} \text{ cm}^{-3}$ heavy holes and $2.2 \times 10^{13} \text{ cm}^{-3}$ electrons for two-band fit.

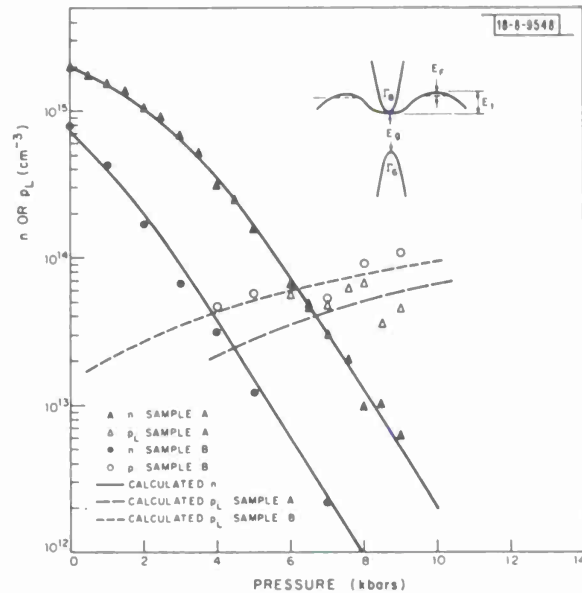
of the semimetal-semiconductor transition at about 8 kbars is given by the sharp rise in the resistivity and the change in sign of the Hall coefficient.

The dependence of the carrier concentrations and mobilities on pressure have been obtained from analysis of the magneto-Hall data, using multiband models. The data obtained at low pressures at 77°K can be fitted well by using a two-band expression for the Hall coefficient, which includes electrons and heavy holes. At higher pressures, where the electron concentration is low, better fits have been obtained by including a third band of light holes. The results of two- and three-band fitting are shown in Fig. III-2 for data obtained at 7 kbars for a sample with $x = 0.14$. At the highest pressures the electron concentration is negligible and the data can be fitted with a two hole band model as shown in Fig. III-2 for the same sample at 9 kbars and 4.2°K .

The electron and light hole concentrations at 77°K , obtained from the analysis, are shown in Fig. III-3 for two samples. The results are compared with calculations based on the Kane model² assuming a momentum matrix element of $9 \times 10^{-8} \text{ eV cm}$. The following values of the parameters* were chosen to fit the experimental data: $E_g = -0.014 \text{ eV}$ for sample A, $E_g = 0.005 \text{ eV}$ for sample B; $dE_g/dP = 7.2 \times 10^{-3} \text{ eV/kbar}$ for both samples; and $E_t - E_F$, which is the height of the Fermi energy above the conduction band edge in the negative gap region, is 0.020 eV for both

* All the parameters are defined in the insert of Fig. III-3.

Fig. III-3. Variation of electron and light hole concentration with pressure in two samples of $\text{Hg}_{1-x}\text{Cd}_x\text{Te}$ at 77°K. For sample A, $x = 0.14$ and for sample B, $x = 0.15$. Lines give carrier concentrations calculated with parameters given in text. Heavy hole concentration remains almost constant with pressure and is $7 \times 10^{17} \text{ cm}^{-3}$ for sample A and $6.2 \times 10^{17} \text{ cm}^{-3}$ for sample B.



samples. E_F is held fixed with respect to the edge of the heavy hole band by the large heavy hole concentration, but there is some uncertainty in its value. By making the simplifying assumption of a parabolic heavy hole band with a density of states effective mass of $0.3 m_0$, a value of -0.005 eV is obtained for E_F and 0.025 eV for E_i .

The warping required to place the Fermi level at the observed position in the conduction band is unexpectedly large. Other models to account for its position are being considered. One possibility is that the slow hole conduction takes place in an impurity band situated above the valence band edge.

C. T. Elliott J. A. Kafalas
J. Melngailis W. C. Kernan
T. C. Harman

2. Observation of Nonextremal Fermi Surface Orbits in Bismuth

Giant quantum oscillations³ in the absorption of ultrasound by a metal or semimetal in a magnetic field, due to the absorption of a single acoustic phonon by an electron which remains on the same Landau level, have been previously observed in several materials.⁴ However, an important property of this type of attenuation – the ability to see nonextremal orbits on the Fermi surface – had not been unambiguously demonstrated. The electrons responsible for most of the attenuation are those whose drift velocities in the direction of the sound wave are the same as the sound velocity. That is,

$$\langle v_H \rangle = \frac{v_s}{\cos \theta} \quad (1)$$

where $\langle v_H \rangle$ is the average electron velocity in the direction of the magnetic field, v_s is the sound velocity and θ is the angle between the magnetic field and the sound wave vector, \vec{q} . Since the Fermi velocity is several orders of magnitude larger than v_s , $\langle v_H \rangle$ will only be appreciably

Section III

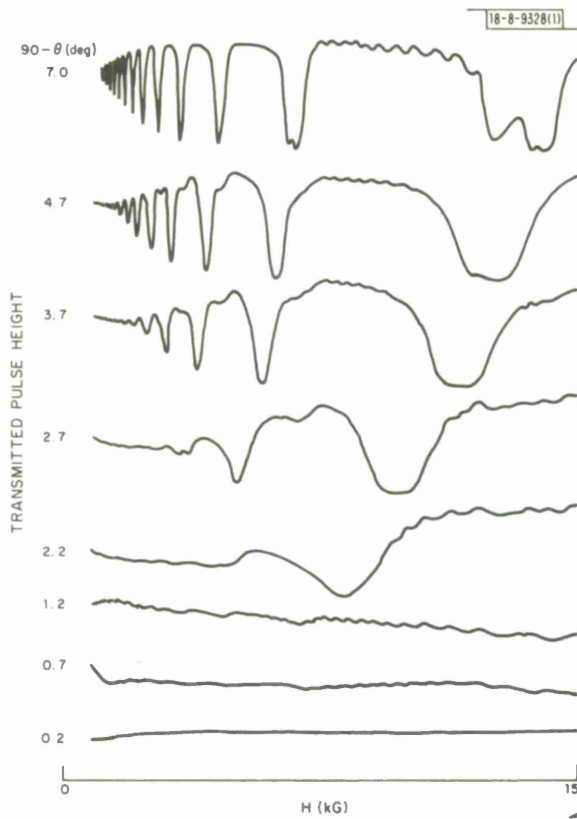


Fig. III-4. Experimental transmitted pulse height versus magnetic field, where θ is the angle between \vec{H} and \vec{q} .

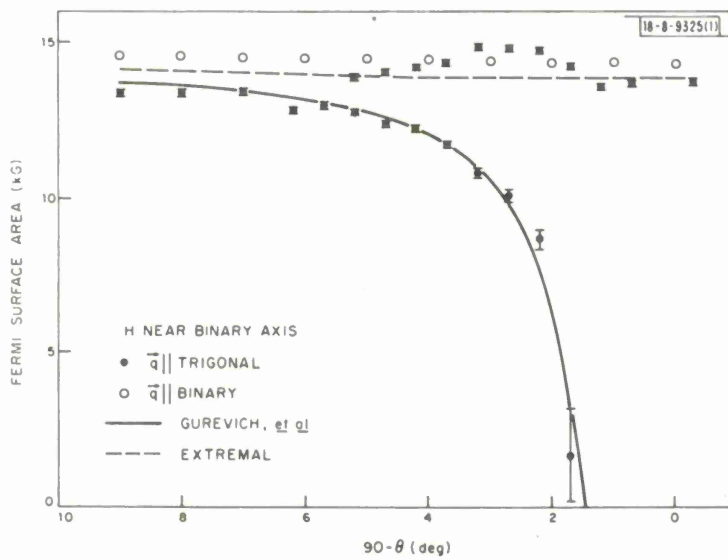


Fig. III-5. Fermi surface areas (in kilogauss). Solid dots are for \vec{q} along trigonal axis, \vec{H} in binary-trigonal plane; θ is angle between \vec{H} and \vec{q} . Open dots are for \vec{q} along binary axis, \vec{H} in binary-trigonal plane; $(90^\circ - \theta)$ is angle between \vec{H} and \vec{q} . Solid line gives predicted nonextremal area, and dashed line gives predicted extremal area.

different from zero when Θ is nearly 90° , so nonextremal orbits should be observable only within a few degrees of $\Theta = 90^\circ$. We have observed simultaneously both extremal and nonextremal areas of the electron Fermi surface in bismuth by studying the attenuation of 185-MHz longitudinal sound waves in a $1 \times 1 \times 1$ -cm single crystal at 1.5°K when $0^\circ < (90^\circ - \Theta) < 10^\circ$.

Figure III-4 shows some of the traces of transmitted pulse height versus magnetic field near $\Theta = 90^\circ$. Sound is propagated along the trigonal axis, and the magnetic field is in the binary-trigonal plane. The large amplitude oscillations that broaden and decrease in frequency with decreasing $(90^\circ - \Theta)$ are due to nonextremal electron orbits, while the smaller ones, which remain fixed in position, are extremal deHaas-van Alphen oscillations.* The Fermi surface areas represented by the two periods are plotted as solid circles in Fig. III-5, along with the theory for extremal (dashed line) and nonextremal (solid line) areas assuming an ellipsoidal-parabolic model for the electrons. The open circles are areas measured with \vec{q} along the binary axis and H near the binary (i.e., Θ is near 0°), where only extremal areas should appear. The small differences in the extremal areas measured in the two configurations, which are outside experimental error, have not yet been explained.

The fact that long period oscillations occur only when \vec{q} is nearly normal to \vec{H} confirms our interpretation that they are due to nonextremal cross sections. Nothing else shows such an angular dependence. Detailed comparison of the lineshapes with theory³ also shows a close resemblance between the two. The only feature not accounted for by the theory is the complete disappearance of even the deHaas-van Alphen oscillations when $\Theta = 90^\circ$. Perhaps measurements of this type will prove a sensitive test of the theory.

This work has been written in expanded form and submitted for publication.

V. E. Henrich
B. Feldman

3. Multi-electron Field Emission

We present a formulation of the field emission problem that takes into account multiparticle emission that results from many-body interactions. We adopt the tunneling Hamiltonian approach and express the two-particle, energy-resolved emitted current in terms of a two-particle correlation function for particles inside the solid. We relate this correlation function to a four-time, two-particle Green's function and show that the current depends only on the bound part of the latter — the free part, which corresponds to independent quasi-particle propagation, gives zero contribution to the current. General features of our results can account for the high energy tail that is observed⁵ in the emission current of some materials.

On the other hand, close scrutiny of the total-energy distributions^{5,6} of electrons from (111)W or (120)W does exhibit a singularity as ϵ , the difference between the energy and the Fermi energy, tends to zero. We believe that such an anomaly at $\epsilon = 0$ may be the consequence of the transient response of the conduction electrons to an abrupt change of potential. An injected hole scattering potential is established suddenly at the time when an electron with energy $E_p < E_f$, the Fermi energy, tunnels; and the Fermi sea has to readjust to a new transient situation. We have

* The high frequency oscillations visible above 5kG are due to other sheets of the Fermi surface and will not be considered here.

Section III

adapted the approach of Nozieres and de Dominicis⁷ to calculate the singular analytic dependence on ϵ of the contribution to the tail current near $\epsilon = 0$.

R. A. Bari
K. L. Ngai

4. Lattice and Correlation Effects on Narrow-Band Electrons

The following is an abstract submitted for the March Meeting of the American Physical Society to be held in Cleveland, 29 March-1 April 1971:

"In a partially filled band, several models have been proposed to account for nonmetallic behavior. We take a unified approach and study a one-band model* that exhibits (in various limits) (a) insulating behavior due to strong correlations, (b) splitting of unoccupied states from occupied states with an accompanying lattice distortion or (c) localization of small polarons at elevated temperatures. We discuss that regime of bandwidth in which small polaron formation and localization due to strong correlations are possible, since several transition-series oxides manifest properties characteristic of both mechanisms."

R. A. Bari

B. MAGNETISM

1. Pyromagnetic Sensors

A preliminary investigation of detecting radiation by means of the pyromagnetic effect has been reported by Caruthers and Walser.⁹ However, they failed to consider leakage flux in their analysis of the magnetic circuit. Figure III-6 depicts a circuit in which a sample S is coupled to a permanent magnet M by means of two yoke pieces Y, with a sensing coil C placed around the

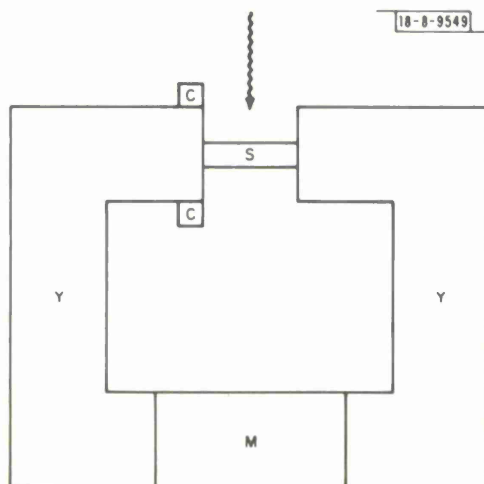


Fig. III-6. The magnetic circuit of a pyromagnetic sensor, consisting of a sample S, a magnetic M, yoke pieces Y, and a sensing coil C.

yoke at the edge of the gap. Let l_i denote length parallel to magnetic field \vec{H} and let A_i denote area normal to \vec{H} . Since it is made of a very soft magnetic material, the yoke can be assumed to approximate an equipotential surface, with a potential difference $U = l_m H_m$ generated across the magnet equal to the drop $U = l_s H_s$ across the sample. Conservation of flux requires that

*Mechanisms (a) and (b) have been discussed from this approach at zero bandwidth in Ref. 8.

$$\psi_m = \psi_s + \psi_g + \psi_l \quad , \quad (2)$$

so that

$$A_m B_m = A_s B_s + (g + G) U \quad , \quad (3)$$

since the flux ψ_g across the air gap and the leakage flux ψ_l are both related to the potential difference U by the purely geometrical factors g and G .¹⁰

At its temperature-field operating point, the sample possesses a differential permeability $\mu_s = \partial B_s / \partial H_s$ and a $\partial B_s / \partial T$, so that

$$\Delta B_s = \Delta T (\partial B_s / \partial T) + \mu_s \Delta H_s \quad , \quad (4)$$

which would cause a change in magnet flux

$$\Delta \psi_m = A_s \Delta B_s + (g + G) \ell_s \Delta H_s \quad . \quad (5)$$

However, the change in flux through the magnet is related to a change in potential across it via the reversible permeability μ_r ; $\Delta B_m = -\mu_r \Delta H_m = -\mu_r \Delta U / \ell_m$, so that

$$\Delta \psi_m = -\mu_r A_m (\ell_s / \ell_m) \Delta H_s \quad . \quad (6)$$

Combining Eqs. (4), (5), and (6), we obtain

$$\frac{\Delta H_s}{\Delta T} = \frac{-(\partial B_s / \partial T) A_s / \ell_s}{g + G + \mu_s A_s / \ell_s + \mu_r A_m / \ell_m} \quad . \quad (7)$$

Now, the flux change linking each turn of the sensing coil will be given by

$$\begin{aligned} \Delta \psi_c &= \Delta \psi_s + \Delta \psi_g = \Delta \psi_m - \Delta \psi_l \\ &= -\ell_s \Delta H_s (G + \mu_r A_m / \ell_m) \quad . \end{aligned} \quad (8)$$

Using Eq. (7), we find that the change in coil flux is related to the change in sample temperature by

$$\frac{\partial \psi_c}{\partial T} = \frac{\Delta \psi_c}{\Delta T} \frac{A_s (\partial B_s / \partial T)}{1 + \left(\frac{g + \mu_s A_s / \ell_s}{G + \mu_r A_m / \ell_m} \right)} \quad . \quad (9)$$

This result shows that the magnetic circuit should be designed to minimize the second term in the denominator.

If radiation is allowed to fall on the sample, a voltage E will be induced in each turn of the sensing coil, with

$$E = 10^{-8} \frac{d\psi_c}{dt} = 10^{-8} \left(\frac{\partial \psi_c}{\partial t} + \frac{\partial \psi_c}{\partial T} \frac{dT}{dt} \right) \quad . \quad (10)$$

The first term represents a reaction from the induced current flowing in the coil and its load and from any eddy currents induced in the yoke. The second term represents the pyromagnetic source of the driving EMF, and

Section III

Fig. III-7. Transmission spectra of $\text{FeSiF}_6 \cdot 6\text{H}_2\text{O}$ using $337 \mu\text{m}$ (upper trace) and $311 \mu\text{m}$ (lower trace) radiation.

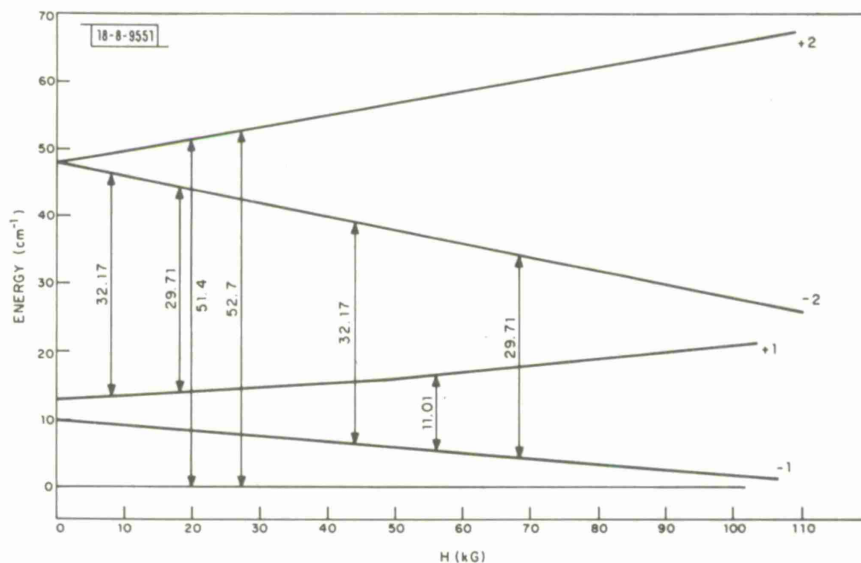
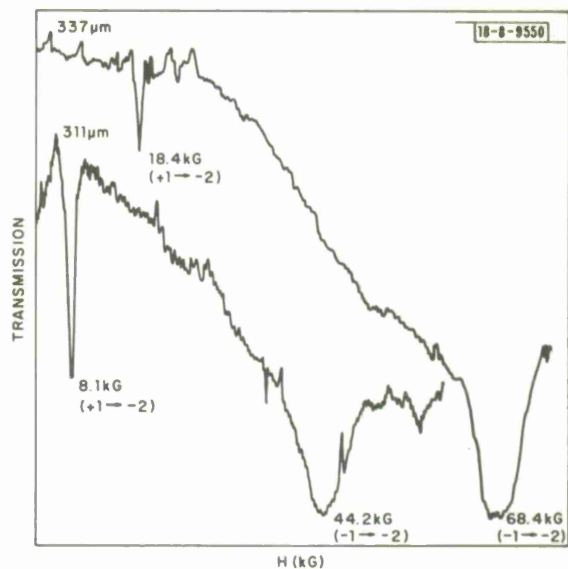


Fig. III-8. Approximate energy level diagram showing observed transitions. The 11.01-cm^{-1} radiation was generated using a CSF carcinotron.

$$\frac{dT}{dt} = \frac{0.238 \alpha P}{\rho c A_s \ell_s} \quad (11)$$

where α is the absorption coefficient, P is the incident power in watts, ρ is the density of the sample, and c is its specific heat. If the incident radiation is subjected to 100 percent square-wave modulation, then Eq. (10) yields the peak-to-peak values of the induced voltages.

We have measured an RMS responsivity of $3 \mu\text{V}/\text{watt-turn}$ in a small coil positioned as shown in Fig. III-6, using a gadolinium sample with $\ell_s \approx 0.063 \text{ cm}$ and $A_s \approx 0.096 \text{ cm}^2$. For Gd, $\rho = 6.3 \text{ gm/cm}^3$ and $c = 0.056 \text{ cal/gm}$. Our magnetometer measurements show that $\partial B_s / \partial T = 550 \text{ gauss/K}^\circ$ and $\mu_s = 2$ at room temperature in an internal magnetic field of 1 kOe ; we estimate an absorption coefficient of about 0.5 cm^{-1} at $0.633 \mu\text{m}$. The biasing field was obtained from a horseshoe magnet having $A_m / \ell_m \approx 0.2 \text{ cm}$ made from Alnico ($\mu_r = 5$), and the Armco yoke dimensions were such that $g \approx 1.2$ and $G \approx 2.9$. (Ref. 10). Consequently, Eqs. (9)-(11) predict an RMS output of

$$\frac{10^6 E_p}{2.8 p} = \frac{10.5}{1 + \frac{1.2 + 3.0}{2.9 + 1.0}} \approx 5 \mu\text{V}/\text{watt-turn} \quad (12)$$

which agrees well with our measured value when allowance is made for the effect of induced currents. The above responsivity is over an order of magnitude greater than the $0.1 \mu\text{V}/\text{watt-turn}$ obtained by Caruthers and Walser⁹ for Gd in their configuration.

K. Dwight
N. Menyuk

2. Paramagnetic Resonance in Ferrous Fluosilicate at Submillimeter Wavelengths

Paramagnetic resonance experiments using submillimeter infrared sources can be used to evaluate new solid state maser materials. In the present experiment single crystals of ferrous fluosilicate ($\text{FeSiF}_6 \cdot 6\text{H}_2\text{O}$) have been studied in transmission at 4.2°K . Although the EPR spectrum had previously been examined at X- and K-bands (Ref. 11), it had never been successfully interpreted.

Typical spectra obtained with the HCN and DCN lasers are shown in Fig. III-7. The spin-orbit interactions remove the fivefold spin degeneracy of the ground state and produce a singlet and two excited state doublets. In the parallel orientation our results can be fitted approximately to a spin-Hamiltonian of the form

$$H = g_{||} \beta H S_z + D S_z^2 + E(S_x^2 - S_y^2) \quad (13)$$

with $S = 2$, $g_{||} = 2.00$, $D = 11.8 \text{ cm}^{-1}$ and $|E| = 0.55 \text{ cm}^{-1}$. The energy levels along with the observed transitions are indicated in Fig. III-8.

As a result of our investigation, apparent discrepancies between EPR and other magnetic measurements in ferrous fluosilicate can now be explained. We find a significant E-term (low symmetry term) in the Hamiltonian which produces a zero field splitting $6E \approx 3 \text{ cm}^{-1}$ of the $M_s = \pm 1$ doublet. This zero field splitting is sufficient to prevent observation of the resonance of this doublet at conventional microwave frequencies.

Since we have successfully determined the low-energy levels of this material for the first time, we are now investigating lifetimes for possible millimeter applications.

H. R. Fetterman
R. S. Rubins*
C. D. Parker

3. High-Temperature Expansion for Magnetic Susceptibility

Recent studies^{12,13} have shown that the first few terms in the high-temperature expansion for the magnetic susceptibility provide the most reliable tool for analyzing experimental susceptibility data in terms of exchange interactions. We have generalized, to an arbitrary number of Heisenberg exchange interactions, the expressions for the first five coefficients in terms of general lattice constants given by Rushbrooke and Wood¹⁴ for a single interaction. When specialized to two interactions, our results agree with those given by Dalton.¹⁵

Let z_i represent the number of neighbors interacting with a given site via an exchange J_i , and define $\alpha_i = J_i / \sum_i z_i J_i$.

$$T\chi/C = 1 + \sum_{n=1}^{\infty} a'_n (\Theta/T)^n \quad (14)$$

$$C/T\chi = 1 + \sum_{n=1}^{\infty} b'_n (\Theta/T)^n \quad (15)$$

where

$$\Theta = (3X/2k) \sum_i J_i z_i \quad (16)$$

$$X = S(S + 1) \quad (17)$$

$$a'_n = a_n / (a_1)^n = -\sum_{m=1}^n b'_m a'_{n-m} \quad (18)$$

$$b'_n = b_n / (-b_1)^n = -\sum_{m=1}^n a'_m b'_{n-m} \quad (19)$$

In the spirit of Rushbrooke and Wood, let $P_{ijk} \dots$ denote the number of distinct vector polygons which can be constructed on a given vector joining a pair of sites that interact via an exchange J_i . Then, in tableau form, the first five b'_n are given in Table III-1. This generalization greatly extends the applicability of the high-temperature susceptibility expansion, since very few materials can be expected to possess only first- and second-nearest-neighbor interactions.

K. Dwight
N. Menyuk

4. Magnetic Phase Transition and Self-Consistent Magnetic Induction in Itinerant Antiferromagnetism

The Fedders-Martin model¹⁶ of itinerant or spin density wave¹⁷ (SDW) antiferromagnetism explains qualitatively the magnetic properties of chromium except for the first-order nature of the transition to magnetic order at the Néel temperature¹⁸ ($T_N = 312^\circ\text{K}$) and the transverse-to-longitudinal spin-flip transition¹⁹ at $T_{SF} = 122^\circ\text{K}$. In the present work, a simple theory is proposed to account for these deficiencies.

* University of Texas at Arlington.

TABLE III-1
TABULATION OF FIRST 5 b'_n COEFFICIENTS

$$b'_1 = -1$$

$$b'_2 = \frac{1}{4} \left\{ \begin{array}{c} 1 \\ 4 \end{array} \begin{array}{c} x^{-1} \\ 3 \end{array} \right\} \Sigma_i a_i^2 z_i$$

$$b'_3 = \frac{1}{10} \left\{ \begin{array}{c} 1 \\ -4 \\ 10 \end{array} \begin{array}{c} x^{-1} \\ -9 \\ 5 \end{array} \begin{array}{c} x^{-2} \\ -6 \end{array} \right\} \left. \begin{array}{l} \Sigma_i a_i^3 z_i \\ \Sigma_{ijk} a_i a_j a_k z_i P_{ijk} \end{array} \right\}$$

$$b'_4 = \frac{1}{80} \left\{ \begin{array}{c} 1 \\ -16 \\ -96 \\ 80 \end{array} \begin{array}{c} x^{-1} \\ 64 \\ -156 \\ 40 \end{array} \begin{array}{c} x^{-2} \\ -45 \\ -54 \end{array} \begin{array}{c} x^{-3} \\ 45 \end{array} \right\} \left. \begin{array}{l} (\Sigma_i a_i^2 z_i)^2 \\ \Sigma_i a_i^4 z_i \\ \Sigma_{ijk} a_i^2 a_j a_k z_i P_{ijk} \\ \Sigma_{ijkl} a_i a_j a_k a_l z_i P_{ijkl} \end{array} \right\}$$

$$b'_5 = \frac{1}{2800} \left\{ \begin{array}{c} 1 \\ 800 \\ -3920 \\ 2464 \\ -4200 \\ -3360 \\ -3360 \\ 2800 \end{array} \begin{array}{c} x^{-1} \\ 80 \\ 7560 \\ 5376 \\ -3150 \\ -3360 \\ -6160 \\ 1400 \end{array} \begin{array}{c} x^{-2} \\ 3570 \\ 9450 \\ 3528 \\ -3150 \\ -315 \end{array} \begin{array}{c} x^{-3} \\ 3780 \\ 2520 \\ 378 \end{array} \begin{array}{c} x^{-4} \\ -1728 \end{array} \right\} \left. \begin{array}{l} (\Sigma_i a_i^2 z_i) (\Sigma_i a_i^3 z_i) \\ \Sigma_i a_i^5 z_i \\ \Sigma_i a_i^3 a_j a_k z_i P_{ijk} \\ \Sigma_i a_i a_j a_k^2 z_i P_{ijk} \\ (\Sigma_i a_i^2 z_i) (\Sigma_{ijk} a_i a_j a_k z_i P_{ijk}) \\ \Sigma_{ijklm} a_i a_j a_k a_l a_m z_i P_{ijklm} \\ \Sigma_{ijkl} a_i^2 a_j a_k a_l z_i P_{ijkl} \\ \Sigma_{ijklm} a_i a_j a_k a_l a_m z_i P_{ijklm} \end{array} \right\}$$

Section III

Associated with the SDW, there is a magnetic induction wave with the SDW periodicity which can be evaluated by solving Maxwell's equations. In this work, we point out that the interaction of the electrons with this magnetic induction wave must be included in the self-consistent determination of the electronic states.

To find the most stable magnetic configuration, we evaluate the free energy of the system, including the magnetic field energy, in the following configurations:

- (a) AF₁: the spin polarization of the SDW is perpendicular to the wave vector of the SDW. In this case, there is a nonzero magnetic induction wave parallel to the spin polarization.
- (b) AF₂: The spin polarization of the SDW is parallel to the wave vector of the SDW. In this case, the amplitude of the magnetic induction wave is found to be zero.

The free energy of the system as a function of the temperature squared is shown schematically in Fig. III-9, with the free energy of the paramagnetic state taken as zero. The free energy

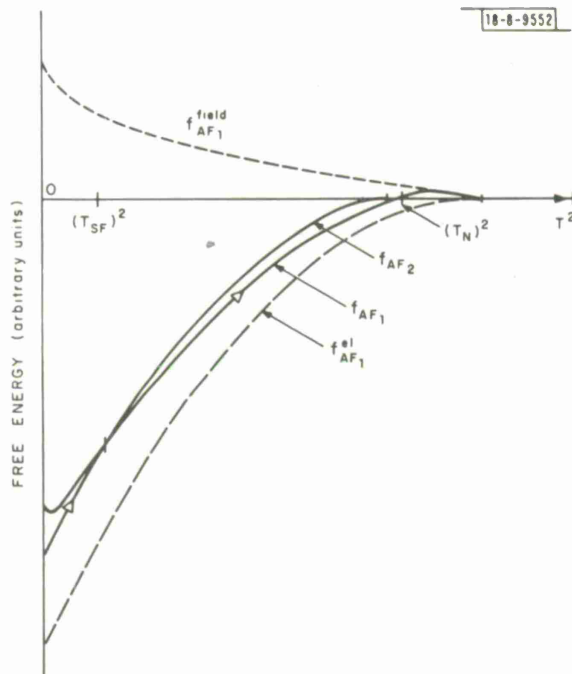


Fig. III-9. Schematic representations of the free energies of the magnetic configurations versus temperature squared. The stable configuration is indicated by the arrows. Detailed description of the symbols used is given in the text.

of the AF₂ configuration is f_{AF_2} . For the AF₁ configuration, the electronic contribution to the free energy is labeled $f_{AF_1}^{el}$, the magnetic field energy is labeled $f_{AF_1}^{field}$, and the total free energy is $f_{AF_1} = f_{AF_1}^{el} + f_{AF_1}^{field}$. As indicated in Fig. III-9, the most stable configurations are:

$$\begin{aligned}
 & \text{AF}_2 && \text{for } T < T_{SF} \text{ ,} \\
 & \text{AF}_1 && \text{for } T_{SF} < T < T_N \text{ ,} \\
 & \text{paramagnetic} && \text{for } T_N < T \text{ ,}
 \end{aligned}$$

since the most stable configuration of the system is the one with the lowest free energy. Notice that the phase transitions at T_{SF} and T_N are first order because the derivative of the free energy of the stable configuration is discontinuous at the transition temperatures. Applied to chromium, the above theory has the proper qualitative features to remove the previously mentioned deficiencies in the Fedders-Martin model.

C. Y. Young
J. W. Allen

5. Spin Wave Approach to Two-Magnon Raman Scattering in Simple Antiferromagnet

A spin wave theory of two-magnon Raman scattering for a simple antiferromagnet at low temperatures has been obtained. The treatment is based on the Dyson-Maleev boson representation of the localized spin operators. At zero temperature, the theory yields results for the Raman cross section which are in excellent agreement with those which obtain from the Green's function equation-of-motion method developed by Elliott and Thorpe.

In the present theory, we derive an approximate cross-section formula in terms of renormalized one-magnon propagators and a vertex function which satisfies a general Bethe-Salpeter equation. Taking into consideration the lowest order interaction processes, it is found that one can satisfactorily account for the experimentally observed shift of the Raman peak to lower energies with increasing temperature. However, it is also found that this lowest-order theory is inadequate for explaining the observed thermal broadening at the Raman spectra.

The possibility that the observed broadening is due to damping of the one-magnon states has been examined, using a phenomenological width Γ for a zone edge magnon. It is found that the necessary width is surprisingly large, although more accurate calculations of the damping of a zone edge magnon are needed to eliminate this possibility. Higher-order irreducible vertex corrections in the two-magnon Bethe-Salpeter equation have also been considered. An approximate cross-section formula which includes these higher-order corrections has been derived using a variational principle. The effect of these corrections on the Raman line shape has not yet been determined.

R. W. Davies
S. R. Chinn
H. J. Zeiger

C. LASER SCATTERING

1. Raman Scattering in FeF_2

We have continued our study of optical Raman scattering in FeF_2 , particularly of the intense line with an excitation energy $\sim 1082 \text{ cm}^{-1}$. As previously reported, this line does not shift position or broaden with increasing temperature, but its intensity lessens and it vanishes at the magnetic ordering temperature, 78.5°K . Broad spectra near this energy remain and become more intense as the temperature is increased.

Our recent studies have included Raman scattering in a magnetic field. In the 180° , back-scattering configuration, with $H \parallel c$, the large xx and yy components of the scattering tensor allowed observation of this line. No obvious effects of magnetic field were seen for fields up to 88 kG. This shows that either both initial and final states have field-independent energies, or that both shift equally. Further studies will be attempted in a larger superconducting magnet permitting a 90° scattering geometry, which should provide better signal-to-noise ratios.

Section III

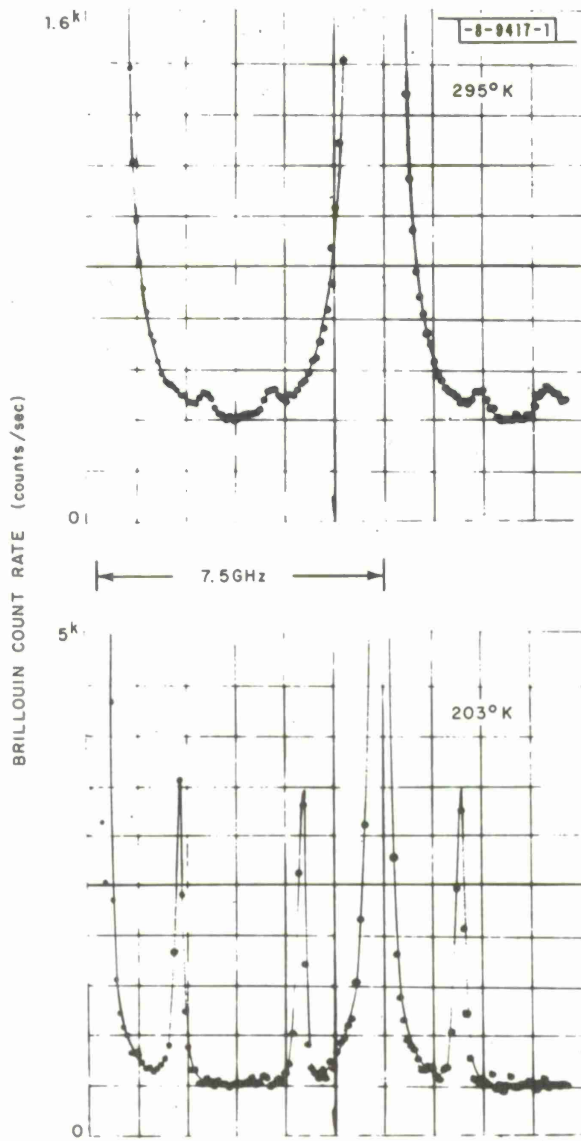


Fig. III-10. Brillouin scattering along c-axis in CdS at 5145 Å.

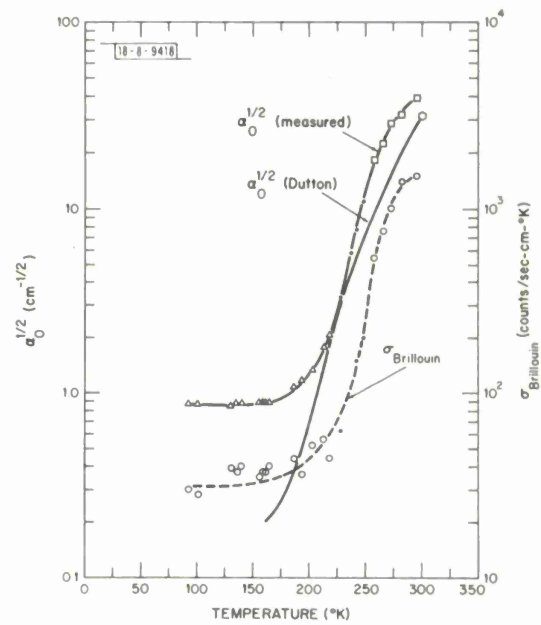


Fig. III-11. Resonant Brillouin scattering in CdS.

Scattering was also observed in another sample of FeF_2 obtained from a different source. Identical spectra were obtained, indicating that impurity effects, possibly from Fe^{3+} ions, are not an important factor in the observed scattering.

A preliminary investigation of the infrared absorption spectrum has shown a line at $\sim 1080 \text{ cm}^{-1}$. Although polarization studies were not carried out, and a more precise calibration needs to be done, this might remove some of the discrepancy between the energy of the 1115 cm^{-1} line observed by Stout²⁰ in absorption, and our Raman scattering measurement.

Further work is continuing on Raman scattering from the crystal field levels of Fe^{2+} ions in other rutile structure host crystals.

S. R. Chinn

2. Resonant Brillouin Scattering in Cadmium Sulfide

A weak resonant enhancement of the Brillouin scattering cross section is observed as the fundamental absorption edge of cadmium sulfide is thermally tuned through the incident radiation at 5145 \AA . The piezoelectrically-active longitudinal acoustic phonon propagating along the c-axis is studied in a backscattering geometry. Signal-averaged Brillouin spectra at $T = 295^\circ$ and 203°K taken with an interferometer of 7.5-GHz free spectral range are shown in Fig. III-10. No multiple phonon lines, reminiscent of resonant Raman scattering in CdS, have been seen. When the measured Brillouin count rate is suitably corrected for the varying temperature and scattering volume, according to the factor $\sigma \sim T(1 - e^{-2\alpha_0 l})/2\alpha_0$ where l is the crystal length and α_0 is the optical absorption constant, the cross section σ is found to increase roughly as the square root of the absorption, as shown in Fig. III-11. This resonant enhancement is less than one would predict on the basis of a theory due to Loudon²¹ but greater than expected from a simple dielectric constant approximation $(\epsilon_{\perp}^2 p_{13})^2 \sim (\epsilon_{\perp} - 1)^2$. Here ϵ_{\perp} is the real part of the ordinary ray dielectric constant at 5145 \AA and p_{13} is the relevant photoelastic Pockel's coefficient. The quantity $(\epsilon_{\perp} - 1)^2$ increases by only about 50 percent over this temperature range.²² Previous resonance photoelastic effects in CdS measured by Tell, *et al.*²³ showed similar results.

The spectral resolution of the experiment is sufficient to observe for the first time a line broadening due to the absorption-induced optical wavevector spread. This is visible in Fig. III-10. Since the phonon frequency is linearly proportional to the wavevector transfer, the wavevector distribution is directly reflected in the excess frequency broadening, $\delta\nu_0$ (line width at half maximum) remaining after instrumental and phonon lifetime widths are subtracted. The optical absorption constant is then given by $\alpha_0 = \pi\delta\nu_0/2v$ where v is the acoustic velocity. The measured absorption constants are in satisfactory agreement with Dutton's²⁴ transmission measurements on thin platelets* in view of possible sample variations. However, the Brillouin determination shows somewhat higher absorptions and a systematic deviation from the Urbach exponential tail usually found in CdS.

A. S. Pine

* These results are also shown in Fig. III-11.

REFERENCES

1. S. Otmezguine, F. Raymond, G. Weill and C. Verie, Tenth International Conference on the Physics of Semiconductors, 17-21 August 1970 (USAEC Division of Technical Information, October 1970) p. 536 and references therein.
2. T. C. Harman and A. J. Strauss, *J. Appl. Phys.* 32, 2265 (1961).
3. V. L. Gurevich, V. G. Skobov and Y. A. Firsov, *Soviet Physics JETP* 13 (3), 552 (1961).
4. For a review, see Y. Shapira in *Physical Acoustics*, Vol. V, W. P. Mason, Ed. (Academic Press, New York, 1968).
5. C. Lea and R. Gomer, *Phys. Rev. Letters* 25, 804 (1970).
6. J. W. Gadzuk and E. W. Plummer, *Phys. Rev. Letters* 26, 92 (1971).
7. P. Nozieres and C. T. de Dominicis, *Phys. Rev.* 178, 1084 (1969).
8. R. A. Bari, *Bull. Am. Soc.* 16, 103 (1971) and *Phys. Rev. B* (in press).
9. R. E. Caruthers and R. M. Walser, "The Feasibility of a Radiation Detection Scheme Utilizing the Pyromagnetic Effect," Technical Memorandum No. 18, 1970, S. S. R. L., E. R. C., University of Texas at Austin.
10. Electrical Engineering Staff of M.I.T., *Magnetic Circuits and Transformers* (Principles of Electrical Engineering Series, the Technology Press, Wiley, New York, 1943), Chapters III and IV.
11. R. S. Rubins, *Proc. Phys. Soc. (London)* 80, 245 (1962).
12. N. Menyuk, K. Dwight and T. B. Reed, *Phys. Rev. B* (to be published, 1 March 1971).
13. Solid State Research Report, Lincoln Laboratory, M.I.T. (1970:3), p. 45, DDC AD-714079.
14. G. S. Rushbrooke and P. J. Wood, *Molecular Physics* 1, 257 (1958).
15. N. W. Dalton, *Proc. Phys. Soc. (London)* 88, 659 (1966).
16. P. A. Fedders and P. C. Martin, *Phys. Rev.* 143, 245 (1966).
17. A. W. Overhauser, *Phys. Rev.* 128, 1437 (1962).
18. A. Arrott, S. A. Werner and H. Kendrick, *Phys. Rev. Letters* 14, 1022 (1965).
19. G. Shirane and W. J. Takei, *J. Phys. Soc. Japan* 17, Suppl. B III, 35 (1962).
20. J. W. Stout, M. I. Steinfeld and M. Yuzuri, *J. Appl. Phys.* 34, 1141 (1968).
21. R. Loudon, *Proc. Roy. Soc. (London)* A275, 218 (1963).
22. D. W. Langer, *J. Appl. Phys.* 37, 3530 (1966).
23. B. Tell, J. M. Worlock and R. J. Martin, *Appl. Phys. Letters* 6, 123 (1965).
24. D. Dutton, *Phys. Rev.* 112, 785 (1958).

IV. MICROELECTRONICS

A. AIR-GAP (BEAM-LEADED) CROSSOVERS

The technique for forming very high density, air-gap crossovers on ceramic substrates has been refined to the point where substrates have been fabricated with greater than 2500 crossovers per square inch with a yield (approximately 99.98 percent) sufficient to give 50-percent good substrates (each good substrate must have 100-percent yield). The technique uses a base metalization of sputtered Ti/Au plated to 0.0003 inch. This metalization is etched to form the basic interconnections, and a layer of Ti/Cu sputtered over the entire substrate and the Cu plated to 0.001 inch, and covered with a flash of gold. The substrate is then spray-coated with AZ-1350H resist and the via holes exposed in the resist and etched in the copper. The crossover pattern is then exposed in the same resist and the crossovers formed by plating gold on top of the copper and through the via holes to a thickness of 0.0005 inch. Finally the resist is stripped and the copper etched away.

This same technique (with the substitution of Mo/Au for the Ti/Au for the interconnect metalization) is being used to fabricate beam-leaded substrates for a 30-stage TTL shift register. The substrate for this circuit is alumina with 36 holes which are formed while the ceramic is in the green state. These holes are filled with glass which is etched out after the interconnections, beam leads and crossovers are formed. Substrates as received have a poor glass-ceramic interface in the hole region, and several substrates have been polished at Lincoln Laboratory in an attempt to create a better surface for thin film processing.

B. SILICON NITRIDE DEPOSITION FOR SIMTOP BY REACTIVE RF SPUTTERING

The properties of silicon nitride (Si_3N_4) formed by RF sputtering in nitrogen were investigated as a function of deposition rate by etch rate measurements and by studying the effect on the nitride of a 1000°C heat treatment in steam. The maximum sputtering rate achieved was approximately 100 Å per minute. This rate was accomplished by using a power density of 4 W/cm² and a sputtering pressure of 3 millitorrs of N₂. Increasing the power did not increase the sputtering rate beyond 100 Å per minute, and the increased power did result in a higher etch rate than the 0.05 Å per second determined for the above sputtering parameters. During the 1000°C wet oxidation, only a small portion of the nitride converted to oxide, indicating that this nitride would be suitable for use with the SIMTOP process. However, tests are under way to evaluate the performance of the nitride during an 1100°C wet oxidation which is the normal temperature used to passivate the sides of the mesa for the SIMTOP process. Further studies are also planned to evaluate the sputtered silicon nitride as a diffusion mask and passivating layer.

C. METAL-BASED, BEAM-LEADED SUBSTRATES

A technique is under development for making inexpensive, flexible beam-leaded substrates using thin (0.002 to 0.005 inch) metal sheet as the base substrate material. The technique involves coating the metal with a dielectric on the circuit side, depositing the interconnect and

Section IV

beam-leaded metalization (usually Mo/Au) on top of the dielectric, plating and etching the gold, forming crossovers if required by air-gap techniques, and etching chip apertures in the dielectric and metal to create the beam-leaded configuration. Three systems of metal and dielectric are under investigation currently. Molybdenum sheet-coated with sputtered SiO_2 has been successfully fabricated into beam-leaded substrates with air-gap crossovers. The only difficulty with this system is eliminating pinholes in the SiO_2 . Tantalum sheet has been pattern-anodized using an evaporated aluminum mask and then SiO_2 sputtered over the entire sheet. This system has no pinhole problems because of the duplex nature of the dielectric, but some difficulty has been encountered in chemically milling the apertures in the tantalum. The last system investigated used a sheet photoresist (generally Dynachem's Laminar) laminated onto copper. The interconnect and beam-leaded metalization is deposited onto the Laminar, and processing proceeds as above. This last process is in the early stages of development.

F. J. Bachner

D. SEMICONDUCTOR PROGRAM

The semiconductor area has been operational for four months, although considerable furnace profiling, equipment adjustment, and tube replacements were required during the quarter due to a power failure. Several of our current projects are summarized below.

TRAPATT Diodes:- A TRAPATT diode project has been initiated for Group 91. Evaluation of commercial silicon planar diodes revealed TRAPATT mode operation under pulse conditions. Evaluation consisted of physical and electrical measurements. Fabrication has been undertaken to produce a silicon mesa diode inversely mounted to operate in the TRAPATT mode under CW conditions. The first units delivered were fabricated on N/N + $\langle 100 \rangle$ silicon wafers with a 6- μm boron diffusion and an I region of 4 μm . The diameter was 5 mils with the capacitance (C) at 0 volts of 2.5 to 3.0 pfs and BV_R of 80 V. The diodes were nickel-gold metalized and flip-mounted in a standard microwave package resulting in a thermal resistance of 50° to 60°C/watt. The effect of wafer orientation, metalization, diffusion depth, I region width, and mounting processes are being evaluated on subsequent runs.

Mixer Diodes:- Further work on GaAs millimeter wave diodes have produced a "best" device with a series resistance of 4 ohms. Evaluation of various material parameters such as epitaxial layer doping and thickness, number of defects, uniformity, and etching properties of pyrolytically and sputtered silicon dioxide dielectric continue to improve the consistency of the electrical properties.

E-Birds:- Continued experiments in processing variables have improved the quality of the silicon dioxide dielectric to the extent that low leakage, channel free junctions have been obtained capable of handling at least 2 W continuous DC input power at avalanche. An improved electron beam shield has been attached to the device but results have not yet been received as to its capability of withstanding the electron beam. Current amplification has already been proven satisfactory. Work is also proceeding on an N diffused P type wafer, as compared to the conventional P diffused N type wafers to determine if electron beam surface inversion will be reduced significantly.

Surface Wave Amplifiers:- Recent processing experiments on annealing, silicon on sapphire, and smooth etching processes have resulted in a 50-percent increase in surface mobility which should increase the efficiency of these types of devices substantially.

Thermal Oxide Passivation:- Varactor diodes have been thermally oxidized, as opposed to pyrolytic oxide with resulting sharp diodes. An undercutting of the oxide resulting in edge leakage problem has been solved by a change in the photoresist techniques for these diodes.

LSI:- Several groups of wafers have been processed to Group 23 specifications for their LSI program. The processing includes, at present, oxidation, boron deposition, and diffusion.

Nuclear Radiation Particle Detector:- A working model utilizing an ordinary silicon wafer has been constructed successfully. The device consists of many active devices on both sides of an extremely thin silicon wafer. Electrical contact is made to the many devices by a combination of gold beam leads and aluminum bonding pads. The actual device is now being constructed utilizing a very high resistivity, 30,000 ohm-cm silicon wafer.

R. A. Cohen

E. MASK FACILITY

The mask facility has continued to progress during the past quarter with refinement of equipment, techniques, and procedures. Difficulties in the procurement of error-free punched paper tapes which have caused significant headaches have been largely worked out, and plans for eliminating paper tapes from the process altogether are in the works. Mask quality is improving and turnaround time is decreasing.

F. PROGRAMMING

In order to reduce the incidence of bad paper tapes, changes have been made in punching and verification with the cooperation of Group 28. Specifically, it is now possible for the first time to read and check the accuracy of a paper tape on the time-sharing system. Normal refinements to the Mann-plot program, consistent with changing demands and with changes in the time-sharing system continue.

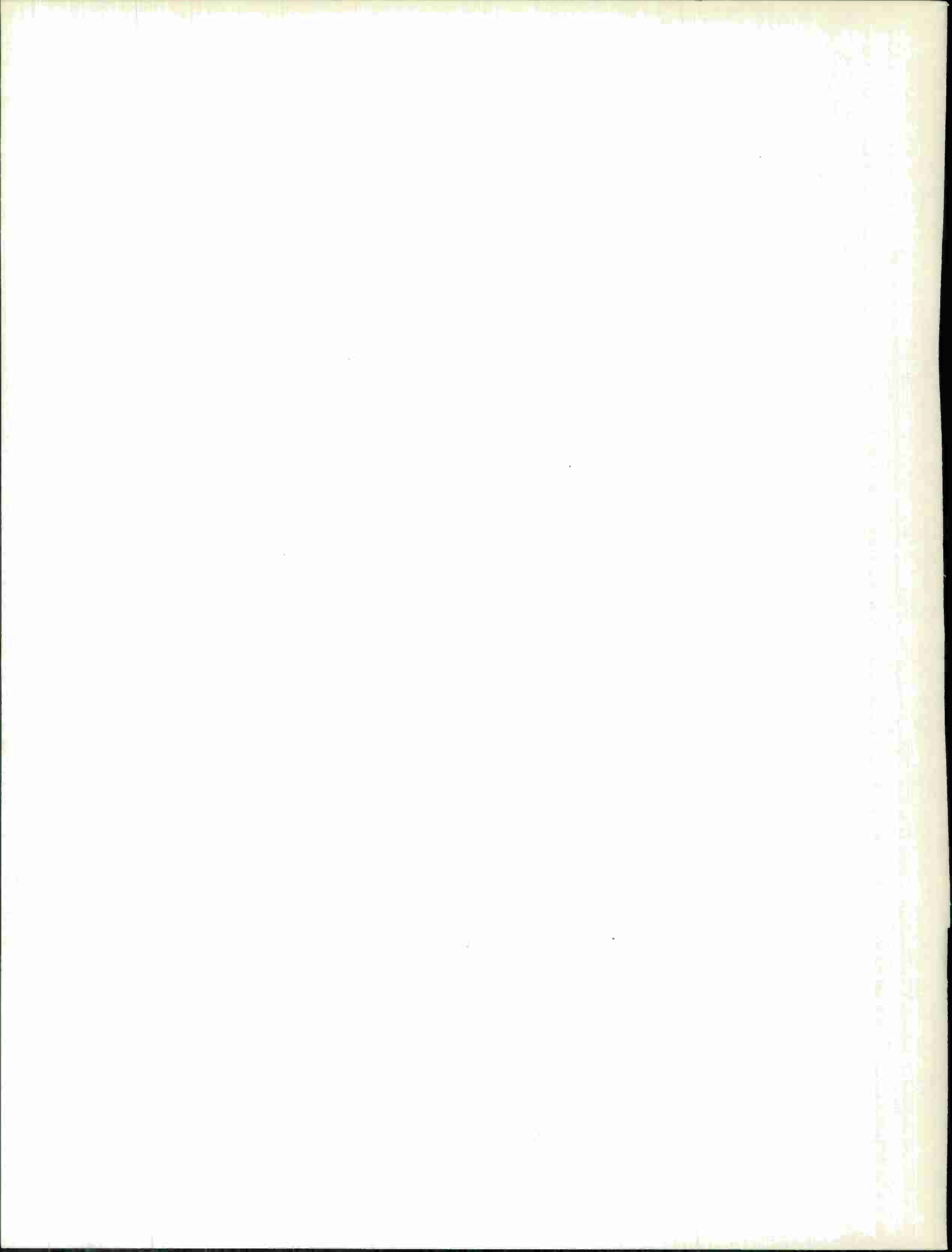
During the past quarter a new system of programs designed to allow generation of masks from a scale drawing has been completed. A digitizer is used to extract coordinates or to trace lines from the drawing which may contain arbitrary curves, rectangles, etc. Virtually any pattern which Group 87's mask generating equipment (D. W. Mann Co. Model 1600A pattern generator) is capable of generating can now be produced using these and pre-existing programs. The programs now existing at Lincoln Laboratory for mask generation provide for unmatched flexibility in the use of this pattern generator.

N. B. Childs

G. BONDING, PACKAGING AND ENVIRONMENTAL TESTING

The design of the 256 diode array proposed as an orientation sensor for LES-9 satellite requires an unusual and rugged package. The basic design of this package has been developed and a model of it subjected to vibration and shake tests to evaluate its suitability to the expected environment. The package and bonding passed these tests successfully. An operating array is being constructed and packaged and will be available for more complete and rigorous testing.

T. F. Clough



DOCUMENT CONTROL DATA - R&D		
<i>(Security classification of title, body of abstract and indexing annotation must be entered when the overall report is classified)</i>		
1. ORIGINATING ACTIVITY (Corporate author) Lincoln Laboratory, M.I.T.	2a. REPORT SECURITY CLASSIFICATION Unclassified	2b. GROUP None
3. REPORT TITLE Solid State Research		
4. DESCRIPTIVE NOTES (Type of report and inclusive dates) Quarterly Technical Summary - 1 November 1970 through 31 January 1971		
5. AUTHOR(S) (Last name, first name, initial) McWhorter, Alan L.		
6. REPORT DATE 15 February 1971	7a. TOTAL NO. OF PAGES 68	7b. NO. OF REFS 71
8a. CONTRACT OR GRANT NO. F19628-70-C-0230 b. PROJECT NO. 649L c. d.	9a. ORIGINATOR'S REPORT NUMBER(S) Solid State Research (1971:1)	9b. OTHER REPORT NO(S) (Any other numbers that may be assigned this report) ESD-TR-71-20
10. AVAILABILITY/LIMITATION NOTICES Approved for public release; distribution unlimited.		
11. SUPPLEMENTARY NOTES None	12. SPONSORING MILITARY ACTIVITY Air Force Systems Command, USAF	
13. ABSTRACT <p>This report covers in detail the solid state research work of the Solid State Division at Lincoln Laboratory for the period 1 November 1970 through 31 January 1971. The topics covered are Solid State Device Research, Materials Research, Physics of Solids, and Microelectronics. The Microsound work is sponsored by ABMDA and is reported under that program.</p>		
14. KEY WORDS		
solid state devices materials research crystal growth magnetism	electronic band structure proton bombardment laser scattering infrared	Raman scattering magneto-optical research microelectronics

